

Chapter 1

Introduction

Metal-oxide surfaces have recently attracted significant attention due to their important technological applications and their potential ability to feature in future devices. The semiconducting properties of metal-oxides make them prime candidates to act as templates for the growth of nano-scale structures. Self-assembled nanostructures grown on “natural templates” are also of much interest for new technological applications [1-6]. There are two main reasons for this intense interest. *Firstly*, further downsizing of electronic devices by means of lithography becomes very difficult and costly. As a result, there is interest in other alternative approaches to fabricating structures at the nanometre scale. *Secondly*, the materials formed by self-assembly are expected to have novel electronic, magnetic and catalytic properties. Thus, self-assembly is potentially a powerful tool for engineering materials with new properties. Metal-oxide surfaces provide interesting templates for such engineering and thus provide the basis for this study.

In particular, tungsten oxides have displayed remarkable physical properties and have been used in a plethora of applications ranging from photochromic windows to gas sensors [7-10]. Tungsten trioxide is a wide bandgap semiconductor which is insulating at room temperature. However, the material readily becomes oxygen deficient to form WO_{3-x} , where x is a variable composition factor. WO_3 is a prototype d^0 oxide based on the framework of corner sharing WO_6 octahedral. The formal oxidation state of tungsten is +6, however due to strong covalency the W (VI) ions do not carry the full 6+ charge. The neighbouring oxide ReO_3 has a simple cubic structure with an Re-O-Re angle of 180° , but in WO_3 rotation and distortion of the WO_6 octahedral give rise to a series of lower symmetry structures [11]. Thermodynamically, tungsten trioxide is the most stable of the tungsten oxides and thus is the final product of oxidation of tungsten metal and of lower tungsten oxides. The ability of the material to become oxygen deficient gives rise to the interesting variation in optical and

electronic properties and provides a strong case for the use of this particular material in the study.

The study focuses on the oxidation of the W(110) surface from the early chemisorbed phases through to the final product of oxidation that is WO_3 . The techniques used to characterize the surface at each oxidation stage are low energy electron diffraction (LEED), Auger electron spectroscopy (AES) and scanning tunnelling microscopy (STM). The theory of the experimental techniques and the background for the study, including a literature survey, is illustrated in chapter 2. Chapter 3 deals with the technical aspects of the experimental setup and gives a detailed description of the equipment involved. Chapter 4 describes the experimental procedure and analysis before finishing the study with conclusions and future work in chapter 5.

The investigation begins with the preparation of the W(110) surface using a well established cleaning technique which involves exposing the sample to oxygen, followed by a series of flash anneals to temperatures reaching 2200 K. Upon obtaining a satisfactory surface, various oxidation conditions are explored and the results are analysed using the techniques previously mentioned. A complete oxidation study of the W(110) surface is performed for the purpose of growing a template for the engineering of nano-structures.

Chapter 2

Background

2.1 Introduction to experimental techniques

2.1.1 Auger Electron Spectroscopy (AES)

Auger Electron Spectroscopy (AES) has developed to become one of the most important and widely used tools for determining the surface chemical composition of conducting and non-conducting samples. The technique is based on the excitation of so-called “Auger electrons”. A beam of Primary electrons with typical energies ranging between 3 and 30 KeV are incident on the surface. The electron beam can be focused and scanned in the nanometer and micrometer range allowing the top-most atomic layers of the sample to be analyzed. A schematic of the process is shown in figure 2.1. In this example a primary electron is incident on the surface with an energy E_p which is greater than the energy of the core electron in the K level. These conditions allow ionization of a K level electron thereby creating a core level hole. To fill this hole, the atom must relax, forcing a transition of a higher level (shown as L1) electron into the core level hole. As a result of the transition the energy difference ($E_k - L1$) becomes available as excess energy which can be used in either of two ways. It can appear as a characteristic X-ray photon of energy ($E_k - L1$) or it can be imparted onto another electron either in the same level or in a more shallow level, whereupon the second electron is ejected. The first process is that of X-ray fluorescence and the second is that of Auger emission. The Auger transition depicted in figure x would be labeled as KL1L2,3. The Auger electrons have a characteristic energy allowing element identification to be determined. The technique supplies information on the elemental composition of the first 2-10 atomic layers [12].

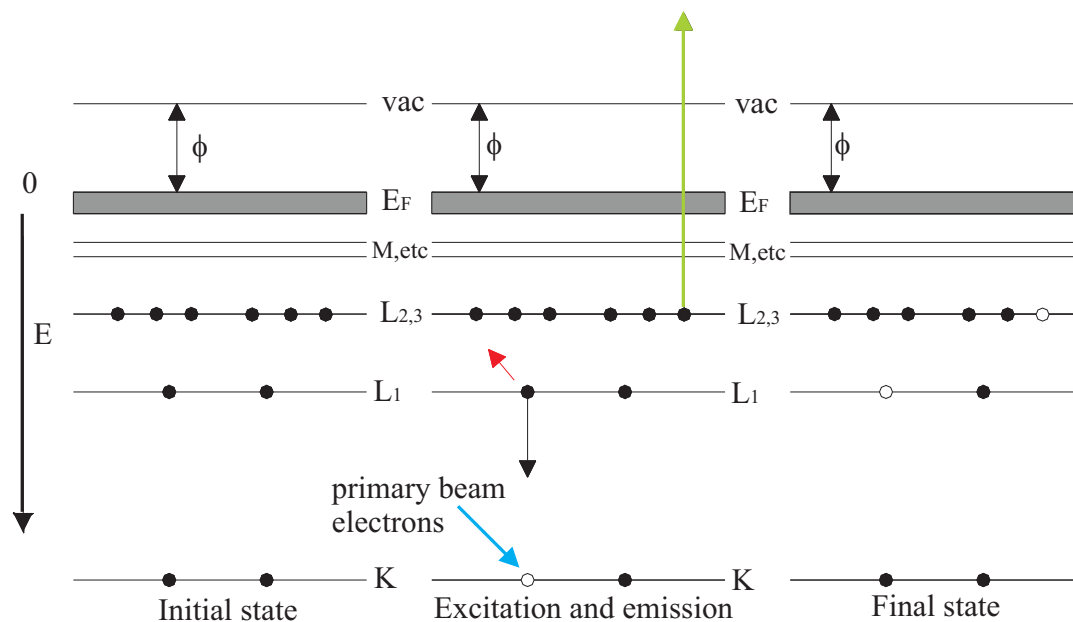


Figure 2.1: The ground state is shown on the left. In the center an incident electron of energy E_p has created a hole in the core level K by ionization. The hole in the K shell is filled by an electron from L_1 , releasing an amount of energy ($E_k - E_{L1}$), which can appear as a photon or can be given up to another electron. The double ionized final state is shown on the right. Reproduced from [13].

2.1.2 Low Energy Electron Diffraction (LEED)

Low Energy Electron Diffraction (LEED) is an important technique in the field of surface science, which allows one to determine the structure and degree of order of a crystal surface [15, 16]. A beam of monochromatic low energy electrons is incident normal to the sample. If the sample has a well ordered crystalline surface then for certain energies the impinging electron beam is elastically back-scattered by the Bragg planes of the crystal. A fluorescent screen is used to capture the back-scattered electrons and display the diffraction pattern of the surface.

The incident electron beam may be regarded as succession of electron plane waves directed at the surface. It is known, that a plane wave incident on an atom or atoms within a unit cell will be scattered in all directions, but interference between waves scattered from

neighbouring unit cells will restrict the net flux to those directions in which the scattered waves from all unit cells are in phase. This requires that the scattered waves from neighbouring unit cells differ only by an integral number of wavelengths λ . For the simple case of a 1-D lattice, the in-phase condition is met for all integers n which satisfy the condition:

$$a(\sin \phi_n - \sin \phi_o) = n\lambda \quad (2.1)$$

where a is the distance between scattering planes, λ is the wavelength of the incident wave and ϕ_o is the angle of the plane wave with respect to the lattice plane, and ϕ_n the angle of the emergent beam with respect to the plane of the crystal. This is known as the Bragg condition. Describing the incident beam and the emergent beam as vectors, s_o and s_n respectively, this can be written as

$$a \cdot (s_n - s_o) = n\lambda \quad (2.2)$$

Or

$$a \cdot \Delta s_n = n\lambda \quad (2.3)$$

Where

$$\Delta s_n = s_n - s_o \quad (2.4)$$

The diffracted beams are determined by Δs_n and, in the one-dimensional case, they are given by integral multiples of the basic unit (λ / a). This involves the reciprocal of the real space vector, a , and thus we define the reciprocal lattice vector $a^* = (1/a)$.

For surface diffraction to occur in a 2D system, with translational vectors h and l , the incident electron beam must conserve both its energy and the component of its momentum parallel to the surface:

$$\vec{k}_{||}^2 + \vec{k}_{\perp}^2 = \vec{k}'_{||}{}^2 + \vec{k}'_{\perp}{}^2, \quad \vec{k}'_{||} = \vec{k}_{||} + \vec{g}_{hl} \quad (2.5)$$

where $k_{//}$ and k_{\perp} are the momentum components of the incident beam, while $k'_{//}$ and k'_{\perp} are those of the diffracted beam. The reciprocal lattice vector, now labeled ghl , is related to the beam energy E_{ev} , the electron mass m_e , and the diffraction angle α by:

$$|ghl| = |h\vec{a}^* + l\vec{b}^*| = |\vec{k}| \sin \alpha = \frac{\sqrt{2m_e E_{ev}}}{\hbar} \sin \alpha \quad (2.6)$$

where a^* and b^* are the reciprocal lattice primitive net vectors. These are related to the real space vectors a and b by [14]:

$$\vec{a} \cdot \vec{a}^* = \vec{b} \cdot \vec{b}^* = 2\pi \quad \vec{a} \cdot \vec{b}^* = \vec{b} \cdot \vec{a}^* = 0 \quad (2.7)$$

This shows the direct correspondence between the observed diffraction pattern and the reciprocal lattice of the surface. The reciprocal lattice vector ghl lies in a direction that is orthogonal to the plane of the real space lattice that is denoted by the Miller indices h and l . The miller indices of the diffracting planes are used to index the diffraction spots of the LEED pattern.

In general, for LEED experiments, the sample is normal to the incoming beam. This means that $k_{//} = 0$ for the incident electrons. Therefore the observed diffraction pattern will be an image of the reciprocal lattice of the surface. LEED patterns of the surfaces are taken at energies ranging between 20 and 500eV. In this energy range the de Broglie wavelength of electrons have the same order of magnitude as the interatomic distances of crystals. The electron mean free path is of the order of $\sim 5 - 10 \text{ \AA}$, meaning that this technique is sensitive only to surface layers.

2.1.3 Scanning Tunneling Microscopy

Comprehensive reviews of the theory and operating principles of scanning tunneling microscopy (STM) are given in dedicated texts by Chen and Wiesendanger [15, 16]. The fundamental theory of STM is modeled on the quantum mechanical description of an electron with energy E traveling in a 1D potential $U(z)$ of the form shown in figure 2.2(a). This electron is described by a wavefunction $\psi(z)$, which satisfies the schrodinger equation:

$$-\frac{\hbar^2}{2m} \frac{d^2}{dz^2} \Psi(z) + U(z)\Psi(z) = E\Psi(z) \quad (2.8)$$

Where m is the electron mass and $\hbar = h/2\pi$ (where h is planck's constant). In the classically allowed region where $E > U(z)$, this equation has solutions of the form:

$$\Psi(z) = \Psi(0)e^{\pm ikz}, \quad k = \frac{\sqrt{2m(E-U)}}{\hbar} \quad (2.9)$$

where the electron can move in either the positive or negative direction. In the classically forbidden barrier region where $E < U(z)$, the schrodinger equation has the solution:

$$\Psi(z) = \Psi(0)e^{-kz}, \quad k = \frac{\sqrt{2m(U-E)}}{\hbar} \quad (2.10)$$

The κ term describes the decay of the electron wavefunction within the barrier region. For a finite potential $U(z)$, there is no non-zero probability P of finding the electron at a position z inside the barrier region, which is given by:

$$P \propto |\Psi(0)|^2 e^{-2kz} \quad (2.11)$$

Consequently, if the width of the tunnel barrier is sufficiently narrow, there is a finite probability that the electron can tunnel through the barrier region.

In the tip-vacuum-sample configuration of an STM junction, the height of the tunnel barrier is determined by the work function Φ of the tip and the sample (assumed to be identical for convenience), which is the minimum energy required to remove an electron from the metal to vacuum. An electron at the tip or sample surface, with Fermi energy $E_f = -\Phi eV$, will have the greatest opportunity to tunnel through the barrier, since by definition the Fermi level denotes the upper limit of electron occupancy in the metal. In the absence of an externally applied bias, the electron can tunnel through the barrier in either direction so that there is no net tunnel current. By applying an external voltage V , electrons in the sample within the energy range $E_f - eV \leq E \leq E_f$ have an opportunity to tunnel through the barrier. If

$eV \ll \phi$, then only electron states very near to the Fermi level are probed. The probability for an electron in the n th states to tunnel through a barrier of width W is given by:

$$P \propto |\Psi_n(0)|^2 e^{-2kW}, \quad k = \frac{\sqrt{2m\phi}}{\hbar} \quad (2.12)$$

Taking all the possible states in the energy range $E_F - eV \leq E \leq E_F$ into account, the tunnel current is:

$$I_t \propto \sum_{E=E_F-eV}^{E_F} |\Psi(0)|^2 e^{-2kW} \quad (2.13)$$

If V is small enough that the density of electronic states does not vary significantly within it, the latter sum can be conveniently written in terms of the local density of states (LDOS). At the Fermi level, at a location z and energy E , the LDOS $\rho_s(z, E)$ of the sample is defined as:

$$\rho_s(z, E_F) = \frac{1}{\epsilon} \sum_{E_n=E-\epsilon}^E |\Psi(z)|^2 \quad (2.14)$$

for a sufficiently small ϵ .

The LDOS is the number of electrons per unit volume per unit energy, at a given point in space and at a given energy. The tunneling current can be conveniently written in terms of the LDOS of the sample at $z = 0$ and $E = E_F$:

$$I_t \propto V \rho_s(0, E_F) e^{-2kW} \quad (2.15)$$

It is clear from this equation that: (1) the tunnel current is directly proportional to the bias applied across the junction, (2) it decays exponentially as the distance between the tip apex and the sample surface is increased.

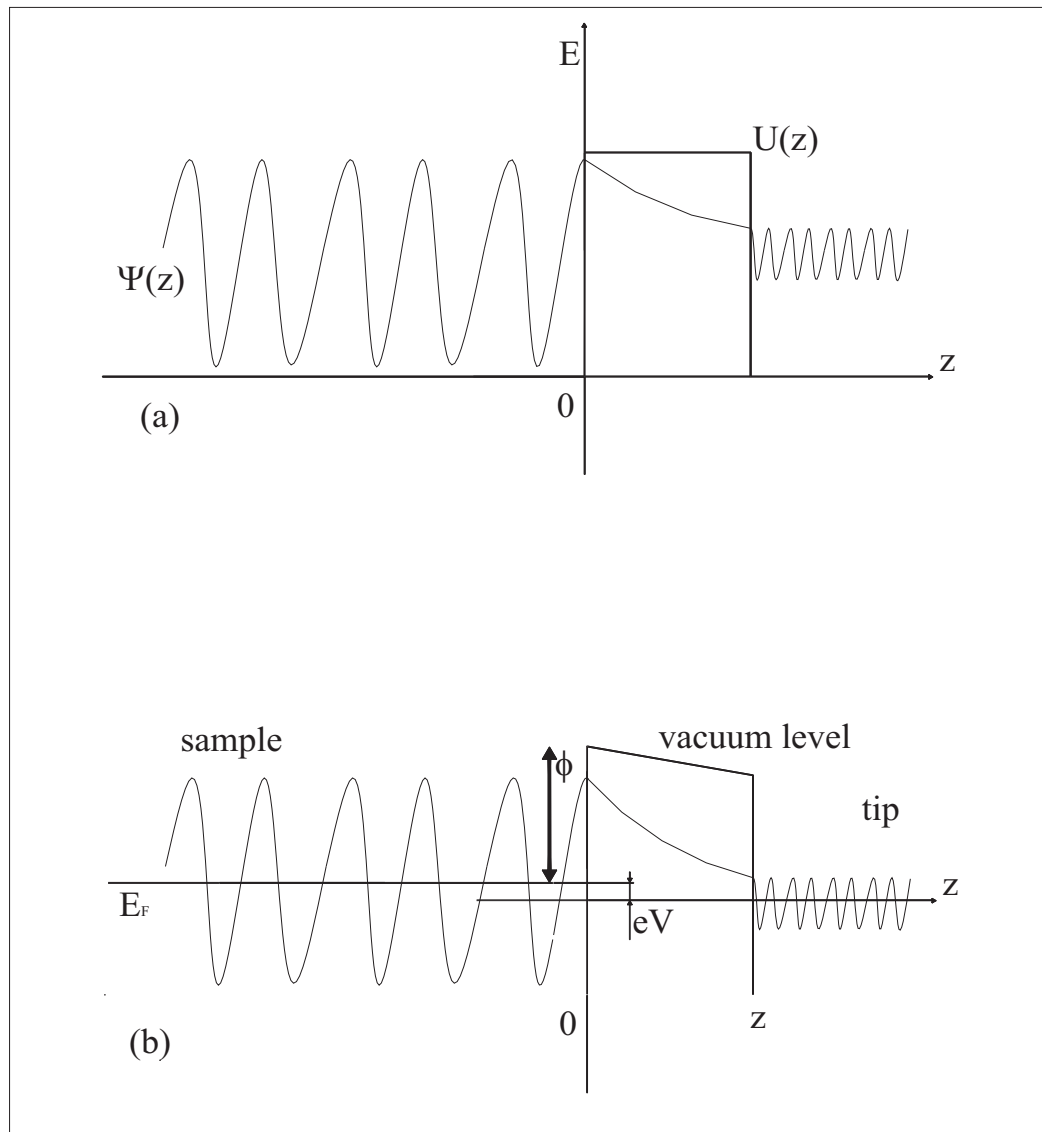


Figure 2.2 Schematic representation of (a) an electron described by the wavefunction $\psi(z)$ traveling in a one-dimensional potential $U(z)$ and (b) a STM junction under an applied bias V .

The significance of the probe-tip LDOS contribution is realized through a time-dependent perturbation model of metal-insulator-metal tunneling proposed by Bardeen [17]. Here, a transfer Hamiltonian H_t is used to describe the transfer of a tunneling electron from a sample state ψ to a tip state χ . The tunnel current can be taken as a convolution of the sample LDOS ρ_s and the tip LDOS ρ_t .

$$I_t = \frac{4\pi e}{\hbar} \int_0^{eV} \rho_s(E_F - eV + E) \rho_t(E_F - E) |M| dE \quad (2.16)$$

It also includes a tunneling matrix element M , describing the amplitude of electron transfer across the tunnel barrier (through the overlap of the ψ and χ states). The integral describing M is evaluated over any surface lying within the barrier region and rate of electron transfer is determined by the Fermi golden rule [18].

$$M = \frac{\hbar}{2M} \int (\chi^* \frac{\partial \Psi}{\partial z} - \Psi \frac{\partial \chi^*}{\partial z}) dS \quad (2.17)$$

Bardeen and Giaever [17] assumed that the magnitude of the tunneling matrix element $|M|$ does not change appreciably in the interval of interest. Thus, the tunneling current is determined by the convolution of the DOS of two electrodes:

$$I_t = \frac{4\pi e}{\hbar} \int_0^{eV} \rho_s(E_F - eV + E) \rho_t(E_F - E) dE \quad (2.18)$$

2.2 Tungsten and its oxides

2.2.1 Introduction

Tungsten is a steel-grey to tin-white metal which was discovered in 1783 by Fausto and Juan Jose de Elhuyar. It has the highest melting point of all the metals (3695 K) and the highest tensile strength at temperatures above 1923 K. The metal oxidizes in air and is obtained commercially by reducing tungsten oxide with hydrogen or carbon. Due to its high melting point, Tungsten is widely used in light bulbs, vacuum tube filaments and electrodes, as it can be drawn out into very thin metal wires. It plays a major role in a variety of other applications spanning from the electrical/heating industry to the machining of tools. Tungsten features the lowest vapour pressure of all metals, very high moduli of compression and elasticity, very high thermal creep resistance and high thermal and electrical conductivity. Tungsten is the most important metal for thermoemission applications, not only because of its high electron emissivity (which is caused by the addition of foreign elements) but because of its high thermal and chemical stability. Some of the properties of Tungsten are shown in table 2.1.

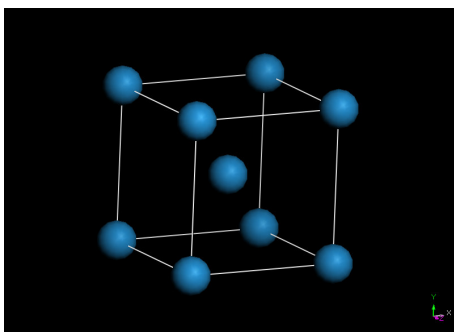
Table of properties	
Atomic Number	74
Average Relative Atomic Mass	183.85±0.03
Electron Configuration	[Xe] 4f ¹⁴ 5d ⁴ 6s ²
Crystal Structure	Body-Centred Cubic A2
Lattice Parameter	a=3.16524 Å (298 K)
Atomic radius (metallic)	137 pm (coordination number 8)
Density	19.25 g/cm ³ (298 K)
Melting Point	3422±15°C
Vapour Pressure (2000°C)	8.15 × 10 ⁻⁸ Pa
Boiling Point	5700±200 °C
Specific heat capacity	135 J·kg ⁻¹ ·K ⁻¹ (298 K)
Enthalpy of fusion	46 kJ·mol ⁻¹
Enthalpy of sublimation	~860 kJ·mol ⁻¹
Coefficient of Thermal Expansion	4.32-4.68 × 10 ⁻⁶ ·K ⁻¹ (298 K)
Electrical Resistivity	5.28 μΩ·cm
Thermal Conductivity Coefficient	1.75 ·W·cm ⁻¹ ·K ⁻¹ (298K)
Modulus of Elasticity	390-410 GPa (298K)
Hardness	300-650 HV30

Table 2.1: Some properties of tungsten

2.2.2 Crystal structure and the W(110) surface

The crystal structure of tungsten is that of body center cubic (BCC) with lattice parameters of 3.16 Å as shown in figure 2.3a. The surface with which experiments were conducted in this thesis is that of W(110) which is a center rectangular unit cell as shown in figure 2.3b. This structure has lattice parameters of 4.48 Å, 3.16 Å and 2.7 Å in the [-110], [001] and [-111] directions respectively. The sample, received from Surface Preparation Laboratory in the Netherlands, was prepared from a 99.995% pure tungsten crystal and was aligned to within $\pm 0.1^\circ$ of the (110) crystal plane.

(a)



(b)

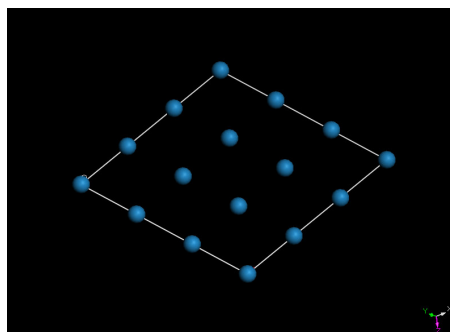


Figure 2.3: (a) Body centred cubic crystal (BCC) structure of tungsten. (b) The center rectangular W(110) surface.

2.2.3 WO₃ and WO₂

Tungsten trioxide is the final product of oxidation and is the most common and commercially accessible compound of tungsten. Other stable tungsten oxides include WO and WO₂ however intermediate states such as W₁₈O₄₉ and W₂₀O₅₈, mainly due to oxygen deficiency, have also been reported. The properties of the numerous oxide states vary significantly and give rise to some very interesting, and potentially technologically advancing, effects. This section will briefly outline some of the most important properties and give a brief description of the crystallographic arrangement of the most common tungsten oxides, namely WO₃ and WO₂.

Tungsten Trioxide

Tungsten trioxide is a wide band gap semiconductor. The bulk unit structure of WO_3 is a WO_6 octahedron with the W(VI) ion at the center. Due to strong covalence, the W ion is not entirely +6 oxidized. This occurrence leads to a distortion of the unit octahedron and correspondingly to a range of bulk phases which vary with temperature as follows:

Monoclinic	to	Triclinic	@	233 K
Triclinic	to	Monoclinic	@	290 K
Monoclinic	to	Orthorombic	@	603 K
Orthorombic	to	Tetragonal	@	1013 K

A particular point of interest is that the monoclinic phase $\gamma\text{-WO}_3$ is stable between 290 and 603 K – the stable phase at room temperature. Stoichiometric monoclinic tungsten trioxide is an insulator at room temperature and has a band gap is 2.6 eV. The crystal resembles that of ReO_3 , and in the monoclinic phase, has lattice parameters of $a = 7.297 \text{ \AA}$, $b = 7.539 \text{ \AA}$, $c = 7.688 \text{ \AA}$ and $\beta = 90.91^\circ$ and belongs to the $\text{P2}_1/\text{n}$ space group. A graphical representation of the WO_3 unit cell is shown in figure 2.4. Tungsten trioxide readily becomes oxygen deficient to form WO_{3-x} which has an effect on the bulk electronic transport properties by introducing donor electronic states into the bulk bandgap. It is due to this electronic effect of WO_3 that the material shows promising potential in the area of gas sensors and electrochromic display devices (discussed more in section 2.3.4).

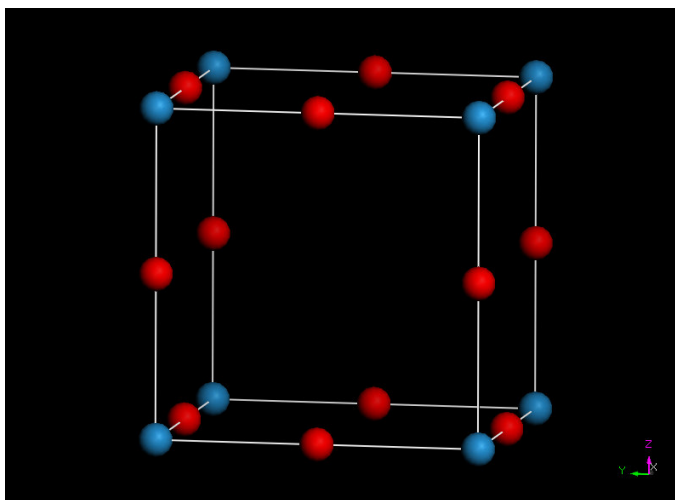


Figure 2.4: Ball and stick model of the ReO_3 -like structure of monoclinic WO_3 . The

Balls represent the oxygen atoms while the blue balls represent tungsten.

Tungsten dioxide

Many metal dioxides, particularly those of the transition metals and namely WO_2 , crystallize in structural types that are closely related to that of the rutile form of TiO_2 . Tungsten dioxide adopts a distorted variant of the rutile structure in which the metal atoms occur in pairs along the c axis of the rutile pseudocell. The rutile structure can be visualized in terms of octahedral WO_6 repeat units which form chains along the c -axis by sharing edges. In tungsten dioxide, deviation from the parent structure is caused by pairing of the tungsten ions within these chains as a consequence of metal-metal bonding. This distortion results in alternating W-W distances of 2.475 and 3.096 Å along the chains and a monoclinic unit cell, with $a = 5.563$ Å, $b = 4.896$ Å, $c = 5.663$ Å, and $\beta = 120.47^\circ$ [61]. WO_2 is conducting at room temperature.

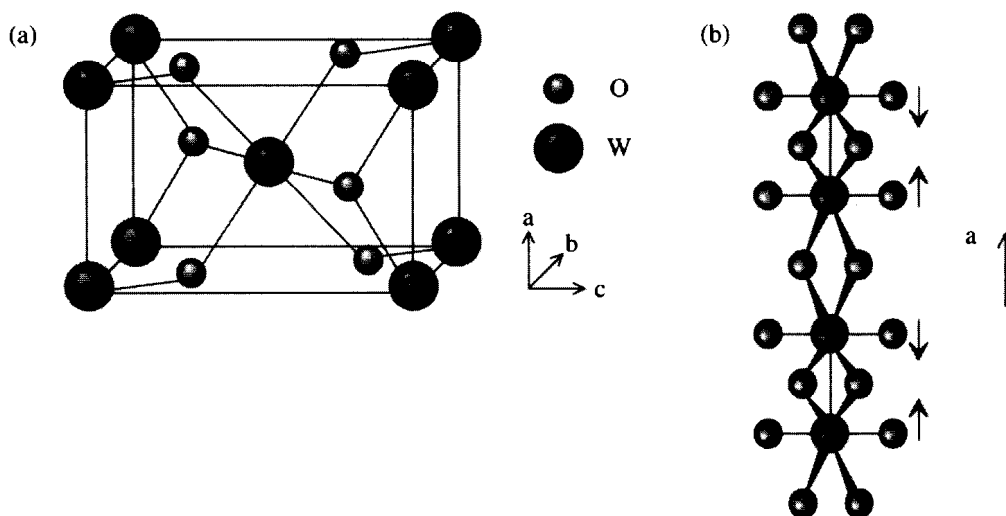


Figure 2.5: (a) The rutile structure on which tungsten dioxide is based. (b) View Perpendicular to the a -axis of WO_2 illustrating the chains of edge-sharing WO_6 octahedral.

2.2.4 Literature review

Oxidation of W (110) has been subject to a wide range of studies spanning many years. Investigations have been executed in the form of two main categories including chemisorption and bulk oxidation of the W (110) surface. A variety of experimental techniques have been employed ranging from surface order studies such as LEED to chemical composition studies such as AES and UPS, to name just a few. This section will

describe an outline of the experimental results achieved to date under the headings mentioned.

2.2.4.1 Chemisorption of Oxygen on W (110)

The main results from a selection of significant studies are as follows: the sticking coefficient of oxygen on W (110) at room temperature was investigated and found to be independent of coverage for small coverage's, decreasing rapidly as with increasing coverage. The value of the sticking coefficient is 0.3 for low coverage [19]. Work function studies were also executed and it was discovered that in general, the work function increases with oxygen adsorption, however, this is true only after an initial period where the work function varies only slightly with increasing coverage [20-23]. Oxygen desorption from the W(110) surface occurs upon heating and a variety of desorption products are observed including O, WO, WO₂, WO₃, and W₂O₆. It was found that the distribution of Oxygen in the products mentioned is strongly dependent on the coverage [24, 25]. It was discovered that a number of ordered structures form on W(110) when exposed to oxygen under various dosing conditions including (2 x 1) @ 0.50 ML, (2 x 2) @ 0.75 ML and (1 x 1) @ 1.00 ML [20, 26]. A number of other studies were performed using techniques such as LEED [19, 27, 28], RHEED [29], AES [30], UPS [31], ellipsometry [32], electron stimulated desorption (ESD) [33,34], field emission and field ion microscopy [21, 35, 36, 37].

The most significant surface study of modern times was accomplished by E. Bauer and T.Engel in a two-part investigation labeled "Adsorption of Oxygen On W(110)", [38, 39]. In this study an effort was made to combine all of the significant previous investigations of the system and hence form a model consistent with all the observations. The first part of the study focused on obtaining data on LEED intensities, work function changes and adsorption kinetics for coverages below 0.5 ML, and subsequently proposed a model for the formation of the p(2 x 1) structure. The second part of the study was concerned with obtaining structural and compositional information on the interaction layer between Oxygen and the W (110) surface for oxygen coverages above 0.5 ML. The techniques included LEED, AES, thermal desorption and work function change measurements. According to this study the adsorption of oxygen on the tungsten surface is subdivided into three coverage ranges: chemisorption, bulk oxidation and an intermediate range which they label as "two dimensional oxidation". The study characterizes the intermediate coverage range between chemisorption and bulk oxidation with respect to the surface structure and composition. It

was discovered that with increasing coverage, complex LEED patterns were observed on heating the oxygenated surface to temperatures in excess of 800 K.

A more recent study focused on the effects of adsorption site and surface stress of chemisorbed oxygen on W (110) for various coverages using Scanning Tunneling Microscopy (STM) [40]. It was discovered that low coverage adsorption results in a gas phase where disordered structures persist while at higher coverages, ordered phases condense with disordered domains. The investigation confirms the adsorption site of oxygen on the W(110) surface to be the triply-coordinated site. At high coverages (~ 1 ML) oxygen adsorbs into two distinct triply-coordinated sites resulting in separate domains with the adsorption site exchanged. The surface compression, created by the adsorption layer, is relieved upon annealing leading to the formation of site-exchanged domain superstructures.

Further investigation into the site-exchanged domain superstructure was accomplished by R.X. Ynzunza et al [41]. A full solid angle photoelectron diffraction with chemical-state resolution study was executed pinpointing the exact local atomic geometry of oxygen adsorbed in the stably saturated one monolayer (1 x 1) structure on W(110). Precise structural determination of the site-exchanged domain superstructure emerged revealing the (1 x 12) periodicity of the mentioned domains.

2.2.4.2 Bulk oxidation of W (110)

A full LEED-Auger oxidation study of W (110) was performed in the 650 – 1100 K temperature range by N.R. Avery [42]. At temperatures in excess of 1000 K, WO_3 (11-1) crystals, faceted to expose {100} type surfaces, are formed. At 850 K, WO_3 (100) crystals in two rotational domains coexist with faceted WO_3 (11-1). At 650 K, no faceted WO_3 (11-1) is formed, but rather an oxide giving rise to an incoherent LEED scatter coexisted with WO_3 (100). It was found that the oxide resulting in an incoherent scatter could be annealed at 1050 K to un-faceted WO_3 (11-1). A model for the nucleation of oxide from a precursor state was developed at the ridges in the metal surface and growth of the bulk crystal was proposed. STM results have been achieved on tungsten oxide surfaces [43-45], however a full STM study of the oxidation of W (110) has not yet been performed.

WO_3 is the final product of oxidation and has shown promising properties and applications which could impact new technological devices. Some of the properties discovered include

electrochromism [46-52], optochromism [53-55] and gaschromism [56, 57]. The material has been used to construct infrared switching devices [47, 58], write-read-erase optical devices [53, 59], electrochromic windows [46, 60-62], gas sensors (NO_2 , Hydrogen Sulfide, Hydrogen, ammonia and O_3) [56, 57, 63-66], and humidity and temperature sensors [66]. A substantial amount of work has been carried out on WO_3 nanoparticles due to their enhanced photochromic effect, where the colour change has been reported to be an order of magnitude faster than that observed in the corresponding bulk material [55]. Photochromic materials, materials that change colour upon going from one oxidation state to another by adsorption of light [67], have potential practical applications in areas such as displays, imaging devices, “smart windows” and solar energy conversion [68-70]. WO_3 and the sub-stoichiometric WO_2 are good catalysts [71-74] and photocatalysts [75]. Some non-stoichiometric oxides WO_2/WO_3 exhibit interesting electronic properties, such as superconductivity and charge carrying [76, 77].

Chapter 3

Experimental details

3.1 The ultrahigh vacuum system

The UHV system was devised and manufactured by Professor I.V. Shvets, Dr. A. Quinn and Dr. J. Osing. It comprises of three main chambers including a preparation chamber, a room-temperature STM (RTSTM) chamber and a low-temperature STM (LTSTM) chamber. The arrangement of the system is shown schematically in figure 3.1. Technical knowledge regarding the construction and operation of the preparation and RTSTM chambers is described by Quinn [78]. A description of the LTSTM and RTSTM can be found in [79, 80] respectively.

The inherent chambers of the system can be isolated via a series of UHV gate valves (VAT [81]) enabling independent pressure control in each. Any one chamber can be brought to atmospheric pressure for maintenance without disturbance in the vacuum throughout the rest of the system. STM tips and samples can be introduced to the system via a fast-entry loadlock which is connected to the preparation chamber through a gate valve. The pressure in the loadlock is conserved in the low 10^{-8} mbar range by a $20 \text{ L} \cdot \text{s}^{-1}$ differential ion-pump (Perkin-Elmer [82]) when idle. Transfer of samples and tips around the system is conducted by a collection of wobblesticks and magnetically-coupled linear drives (Vacuum Generators Ltd. [83]), providing access to all available and necessary locations. The pressure in each chamber is monitored using nude Bayard-Alpert type ionization gauges (Perkin-Elmer). The entire system is supported on a stainless steel box-section frame which can be floated on pneumatic dampers for vibration isolation from the surroundings during STM operation. The box-section is filled with gravel to minimize hollow pipe vibrations.

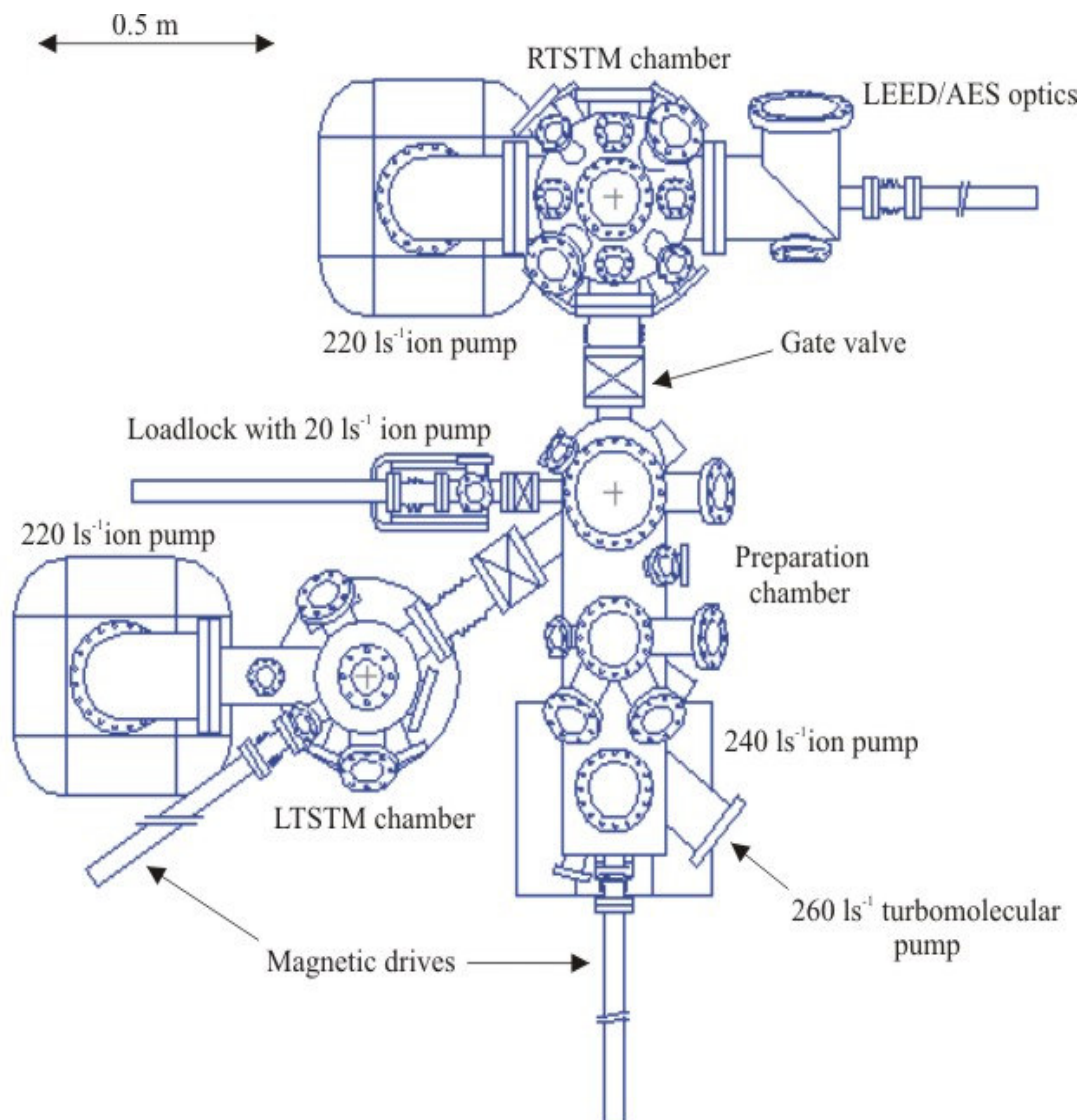


Figure 3.1. Top view schematic of the ultra high vacuum system (UHV) system.

3.2 The preparation chamber

The preparation chamber was designed by Dr. Shane. Murphy [80] and constructed by Caburn-MDC Ltd [84]. It is a standard O.D. 457 mm commercial chamber (Perkin-Elmer) with two modified ports and a total of twenty-one ports altogether. Achievement of UHV conditions requires baking the system for three days at 120°C. A customized back-out tent was designed by the author and manufacturer by [84]. The base pressure achieved after the baking process is in the mid $\sim 10^{-11}$ mbar.

A collection of pumps are used to achieve UHV conditions in the chamber: The first is a TMU 260 L · s⁻¹ turbomolecular pump (Pfeiffer Vacuum [85]). This pump is supported by a 0.7 L · s⁻¹ two-stage rotary vane pump. A double ended 240 L · s⁻¹ differential ion-pump (physical electronics [82]) is used to maintain UHV conditions after the other mentioned pumps have reduced the pressure sufficiently. A liquid nitrogen cryoshroud is inserted in the base flange of the ion-pump which houses a titanium sublimation pump (TSP). A non-evaporable getter pump (NEG) from SAES getters [86] is positioned mid-way along the chamber. This pump is particularly effective at pumping hydrogen.

The preparation chamber contains all the facilities for *in-situ* tip and sample preparation: electron-beam and resistive heaters, a triple evaporator with integral flux monitor, quartz crystal deposition monitor (Inficon [87]), ion gun (VG [88]) and precision leak valves for the controlled introduction of high purity oxygen, hydrogen and argon gases. In addition, the preparation chamber also contains a cylindrical mirror analyzer (CMA) based AES subsystem (Perkin-Elmer) for sample characterization. A detailed description of the main sample preparation facilities used for the preparation and analysis of the crystals are covered in this thesis are given below.

3.2.1 The e-beam heater

The e-beam heater is used for high temperature preparation procedures. It was designed and assembled by Dr. J. Osing [79] and its schematic is shown in figure 3.2. The sample holder is mounted into a Ta stage which is held at a potential of +1 kV. A current ($1.5 \text{ A} \leq I \leq 4.5 \text{ A}$) is passed through a grounded thoriated tungsten filament ($\Phi = 0.15 \text{ mm}$, 1 % Th), which generates thermionic emission of electrons. These electrons are accelerated towards the cap of the sample holder, whereupon collision, their kinetic energy is transferred to the sample as heat. Because the filament is situated to one side of the sample there is a temperature gradient across the sample. Surface temperatures are measured through a window port from outside the chamber using an infra-red pyrometer (Altimex UX-20/600 [89]). The pyrometer operates in the 1 μm range which gives a transmission of 95% through the Kodial window. The e-beam heater was the primary heating device used for both cleaning and annealing the sample during oxygen exposure.

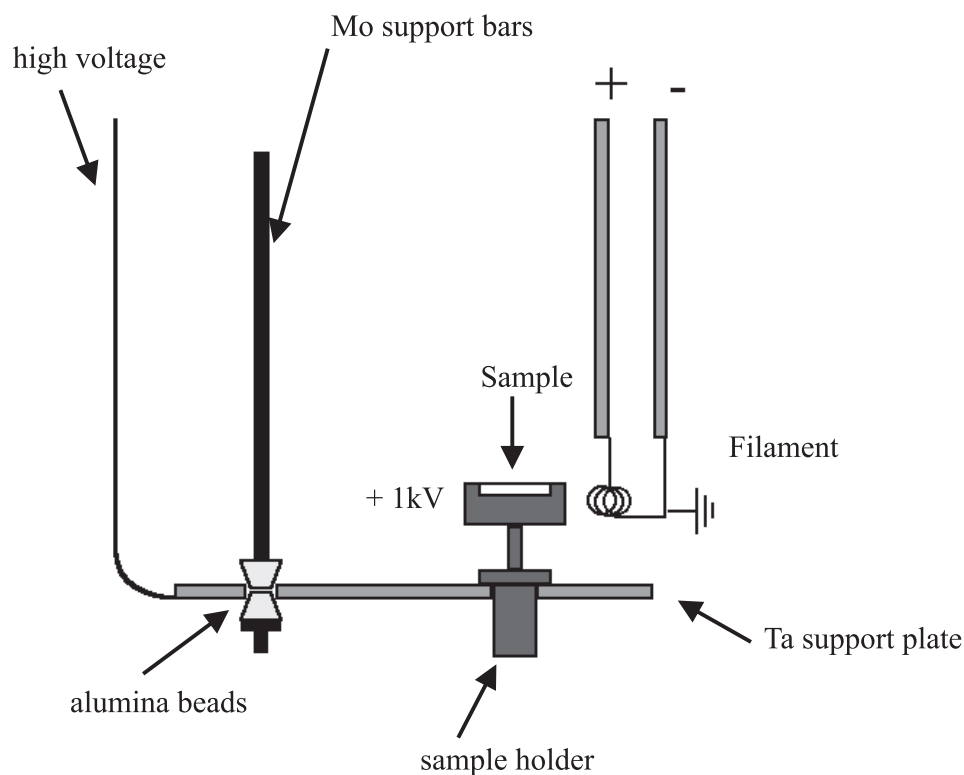


Figure 3.2. Schematic illustration of the e^- -beam heater

3.2.2 The ion gun

The preparation chamber is equipped with an inert sputter ion source (PSP vacuum technology [90]), which is used for Ar^+ ion etching of STM tips and in-situ cleaning of samples. There are two tungsten filaments, through which typical currents of 2.6 A run. The Argon gas is introduced through a leak-valve directly into the gas cell of the ion gun, and ionized by electron bombardment. The base pressure in the chamber rises to $5 \times 10^{-6} \leq P_{base} \leq 1 \times 10^{-5}$ mbar during such an event. A bias voltage of 0.5 to 2keV is applied to the target during bombardment. Discharge currents of vary from 30-40 mA. The target diameter is taken as 11 mm, which is the diameter of the circular Ta insert in the resistive heater, into which the sample/tip is mounted for ion-etching. A thermocouple mounted to this insert allows the target current to be measured. The target current is typically of the order of $8.0 \leq I \leq 20.0 \mu A$ for a 0.5-2keV beam energy and a chamber pressure of 1×10^{-5} mbar.

3.2.3 Auger electron spectroscopy set-up

The Auger analyzer is a cylindrical mirror analyzer (CMA, model 10-155A Physical Electronics [82]). A graphical representation of the analyzer can be seen in figure 3.3. The primary electron beam is generated from a hot filament source, and accelerated through a potential V_2 . It is possible to vary the beam current by changing the extraction potential V_1 . The electron gun is situated between two concentric cylinders, one of which is grounded (inner), and the other (outer) used to deflect the beam. The deflecting potential is chosen such that only electrons of a particular energy will pass through the exit aperture. An electron multiplier is used to amplify the analyzer current before the signal reaches the collector. Primary electrons of known energy, reflected from the sample, are used to optimize the signal intensity to find the analyzed spot and hence enable the analyzer to be calibrated. Further information on the operation of the Auger analyzer can be found in [91]. A beam energy of 3keV was used for all measurements. The filament and emission currents were 3.2 A and 0.4 mA respectively, given a target current of $\sim 8 \mu\text{A}$. A SR 850 DSP lock-in amplifier from Stanford research systems [88] was used to output a 0.5 V_{rms} sinusoidal signal of frequency 12 kHz to modulate the deflecting voltage applied to the outer cylinder. A lock-in sensitivity of 100 μV was used to detect the Auger signal. The scan speed was always set at 1 eV.s⁻¹.

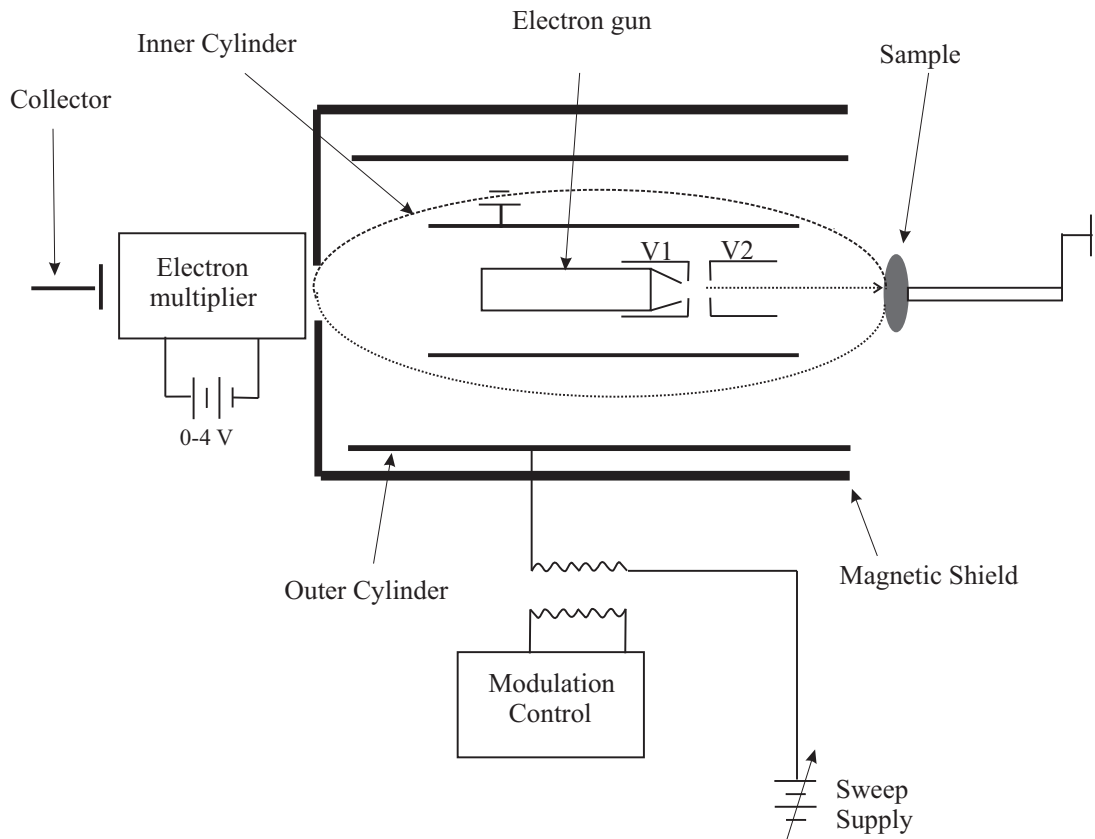


Figure 3.3. Graphical representation of the cylindrical mirror Auger analyzer

3.3 The room-temperature STM

All Acquired STM images were obtained by scanning a tungsten tip across the sample surface in constant current mode. In this configuration the separation between the tip and the sample is maintained by means of a feedback loop which controls a piezoelectric tube scanner. The STM head is constructed of macor and comprises of a piezo tube scanner and a fine approach walker see figure 3.4. It is based upon the system developed by Dr. S.H. pan at the University of Basel, Switzerland [92]. In this design the sample is mounted on a cylindrically polished sapphire rod which is clamped between a set of six piezo stacks, mounted in a triangular fashion. One pair of piezo stacks is spring-loaded against the sapphire rod. The motion of the rod occurs in two steps: first the stacks deform quickly in one

direction and slip under the rod without altering the rods x and y positions. All six piezo stacks then relax simultaneously, dragging the rod with them.

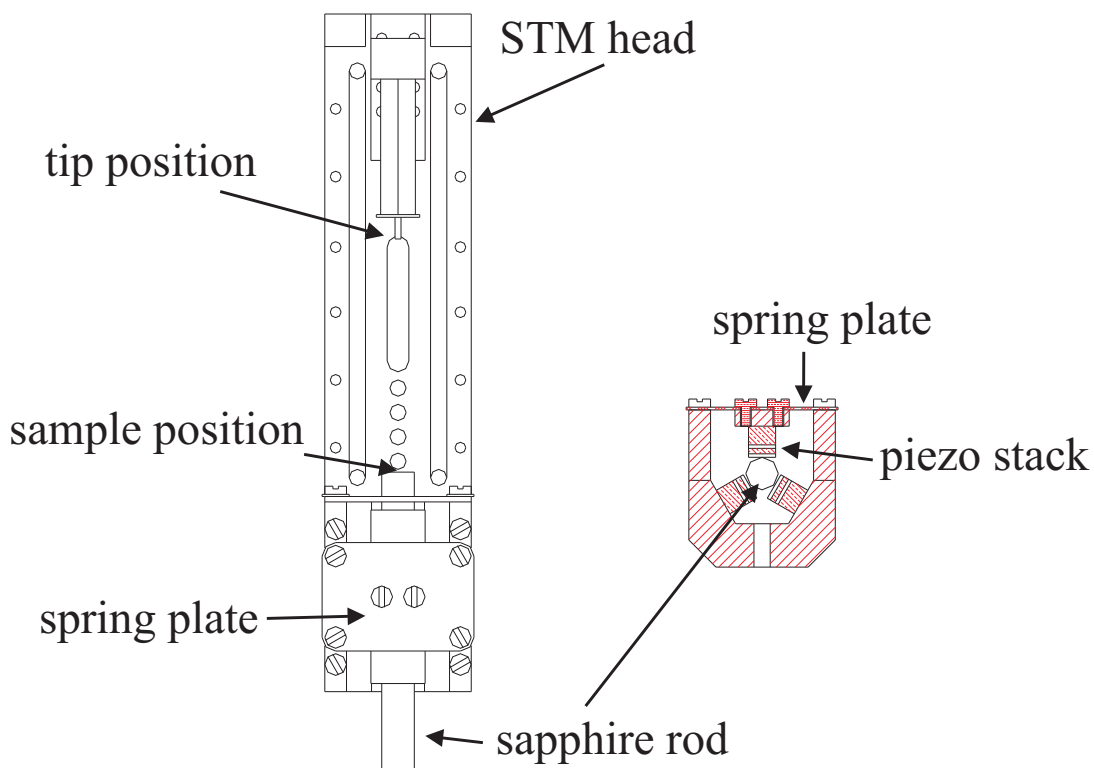


Figure 3.4. Schematic of a STM head similar to the RT-STM. A front view and a cross section of the fine approach walker are shown

Vibration Isolation system

One of the most essential aspects of any STM system is its ability to maintain a tunneling gap of a few angstroms between the tip and the sample. In order to achieve this, the STM must be decoupled from external vibrations (Pohl 1986), giving rise to the need for a vibration isolation system. There are a couple of conditions that must be fulfilled in order to achieve an effective STM system that is insensitive to external vibrations. *Firstly*, the STM head should have a high resonance frequency (> 1 kHz) i.e. it should be light, small and rigid. Typical resonance frequencies should be between 4.5 kHz and 9 kHz as suggested by Taylor [93], for tube scanners similar to the ones used in these measurements. *Secondly*, the STM should be mounted on a vibration isolation system in order to minimize vibrations. Modern STM's use coiled-spring systems (Binnig and Rohrer, 1983) with eddy-current damping or viton-metal stack isolators (Gerber et al., 1986), which consist of stacks of metal plates separated by

layers of Viton. There is the disadvantage of these systems being susceptible to building vibrations due to their resonance frequency range of 10-100 Hz. In order to overcome this problem, it is common practice to “float” the system on pneumatic dampers. Spring systems can be designed with resonance frequencies of 1 Hz or lower but don't provide much damping. For this reason, eddy current damping is usually used in conjunction with these systems.

The entire UHV system used in these experiments is isolated from its surroundings by means of pneumatic dampers. The STM sits on the inner stage of a two-stage coiled spring system, which is mounted to the base flange of the RTSTM chamber. Three outer springs are suspended from stainless steel rods, which are screwed into the base flange. The middle stage of the system is a stainless steel ring (O.D. 154mm, I.D. 139 mm, thickness 20mm). Three titanium rods are screwed into the ring and the inner rings are suspended from near the top of the rods. Both the inner and outer spring suspension mounts can be adjusted up and down to level the system. The STM and I-V converter are bolted to the inner stage, a macor disk of diameter 123 mm and thickness 12 mm. Viton rings attached to both ends of the inner and outer rings provide some damping. The middle stage can be clamped for tip or sample exchange using a wobble stick. Vibration isolation is somewhat disrupted by the fact that there are a number of wires and coaxial cables connected between the outer and inner stage of the damping system. In this sense, improving the efficiency of the spring system may not have a noticeable effect on vibration isolation. However, in practice, the system proved to work quite well.

Fine approach

Typical tip-sample separation distances are required to be of the order of $\sim 5 \text{ \AA}$, making it a real engineering challenge to devise a system with the technology capable of producing such precision. The challenge lies in the ability of the technology to progressively decrease the tip-sample distance without the tip “crashing” into the sample. Binnig and Rohrer (1983) used a “louse” piezo walker which moved by electrostatic clamping and piezo expansion similar to the commercial Inchworm actuators (Burleigh Instruments). The fine approach system used in the STM is a six-leg piezo walker designed by Dr. S.H. Pan at the University of Basel. In this design, the sample is mounted on a quasi-cylindrical polished sapphire rod. Six shearing piezos drive the rod toward or away from the tip.

Tube scanner

The piezoelectric tube scanner has four outer electrodes, of equal area, parallel to the axis of the tube. The inner electrode is grounded, so that when a voltage is applied to one of the electrodes the tube scanner bends away from that electrode. The scanner has a dynamic range of $\pm 13000 \text{ \AA}$ in the z-direction and $\pm 20600 \text{ \AA}$ in the x- and y- directions. These directions were calibrated on Cu(100) monatomic steps and HOPG atomic resolution images respectively. The STM head is isolated from vibrations by a two-stage spring system [78] which works in conjunction with the pneumatic dampers on the frame of the system.

STM Control

For the STM used in this study the junction bias voltage was applied to the sample. Therefore all junction bias voltages, V_b , are stated for the sample with respect to the tip. The STM controller used for experiments is a SCALA system developed by Omicron [94]. This controller allows the user to compensate for thermal drift using a photographic feature of the STM image as a reference point. The accompanying software provides an interface with functions for data analysis. Data was also analysed using commercial software from Nanotecc Electronica S.L. [95].

3.3.1 Low Energy Electron Diffraction Set-up

The RVLO 900 four-grid reverse view optics used in experiments was manufactured by VG Microtech. The optics were mounted on a O.D. 200 mm CF custom elbow which is tilted at an angle of 30° to the horizontal. The sample sits in the transfer fork of a magnetic drive, which is grounded by a stainless steel braid to an OFHC copper block at the bottom of the LEED annex. The sample is rotated in the drive so that its surface faces the electron gun. Scattered electrons are collected by the grids and screen located behind the gun.

A schematic illustration of the four-grid LEED system is shown in figure 3.5. It consists of an electron gun, providing a collimated beam of electrons, and a hemi-spherical fluorescent screen on which the diffracted electrons are observed. The grid nearest the sample M1 is earthed so that the electrons scattered by the sample, initially travel in field-free space. A negative potential is applied to the two center grids M2a and M2b, to suppress inelastically scattered electrons, while those that are elastically scattered are accelerated towards the

phosphorescent screen by its +5 keV potential. The fourth mesh M3 is also grounded to reduce the field penetration of the suppressing grids by the screen.

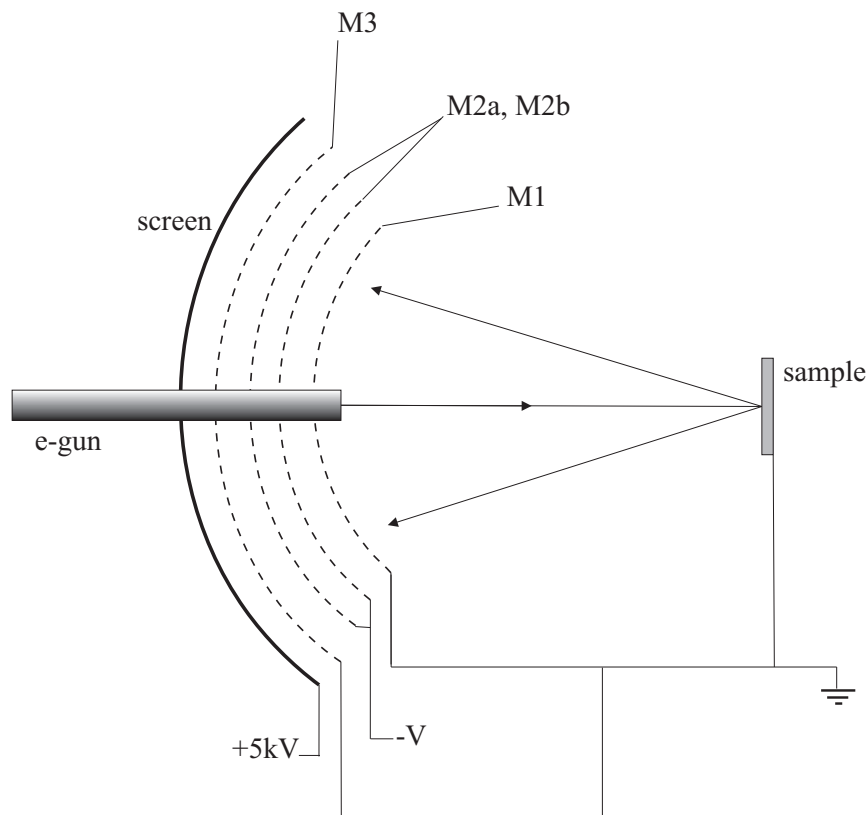


Figure 3.5. Schematic of the four-grid optics operating in LEED mode

LEED patterns of the metal surfaces were captured at energies between 35 and 300 eV, using an emission current of 0.52 mA. The patterns were recorded by photographing the screen with both a digital camera and a CCD. The angle α may be determined from the spot separation d_r between indexed spots in the LEED pattern by using the geometry of the LEED screen, shown in figure 3.6. The actual spot separation can be calculated from the distance d_{photo} measured in a photograph of the pattern if a calibration photo of the entire screen is taken, using:

$$d_r = \frac{d_{photo} D_r}{D_{photo}}$$

Where D_r is the actual screen diameter and D_{photo} is the screen diameter measured in the photograph.

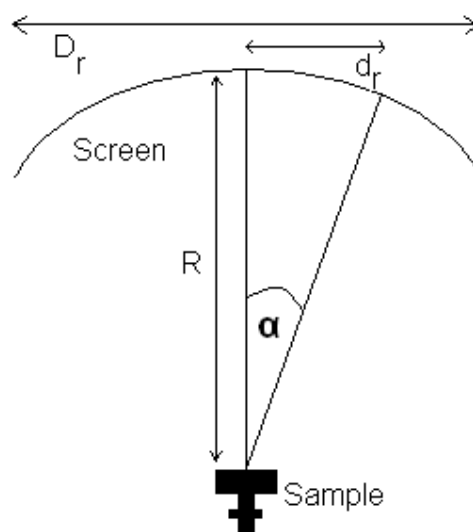


Figure 3.6. Schematic of the LEED screen geometry. The sample is placed at the focal point of the screen. The angle α can be determined from $\tan \alpha = d_r/R$. The distance d_r is the separation between the hk spot and the specular spot

3.4 STM Tips

Atomically sharp and stable tips are of vital importance for achieving atomic scale resolution using STM. Due to its relative hardness, Tungsten is the most widely used material for tip preparation, as it is a stable probe material. Tungsten can be electrochemically etched, enabling the preparation of atomically sharp tips. All STM images in this thesis were obtained using W tips.

W Tips

Tungsten tips are prepared from $\varnothing = 0.5\text{mm}$ W wire. The wire is cut into small rods and an insulating layer, PTFE tubing, is placed on the end of the rod. The rod is then clamped into a modified micrometer screw gauge, which allows precise positioning of the rod in a beaker of 2.0 M NaOH solution. The W wire acts as the anode while a submerged metal foil acts as the cathode. Under an applied 4 V dc bias, chemical etching occurs at the air/electrolyte interface. The tungsten oxidizes to form soluble WO_2^{2-} , which flows away from the active etching region. This leads to a thinning of the wire at the interface region, and eventually the

submerged section of the wire falls off under its own weight. During the etching process the PTFE acts to physically restrict the active etching region [96] and also protects the tip that falls into the beaker [97]. This tip etching setup is shown in figure 3.7. The tips are then lightly rinsed with propanol-2-ol, placed in tip holders and inserted into UHV. Before the tips are used for imaging, they are etched with AR+ ions to remove the WO₂₋₄ present from the chemical etch process. This process produces stable, atomically sharp tips.

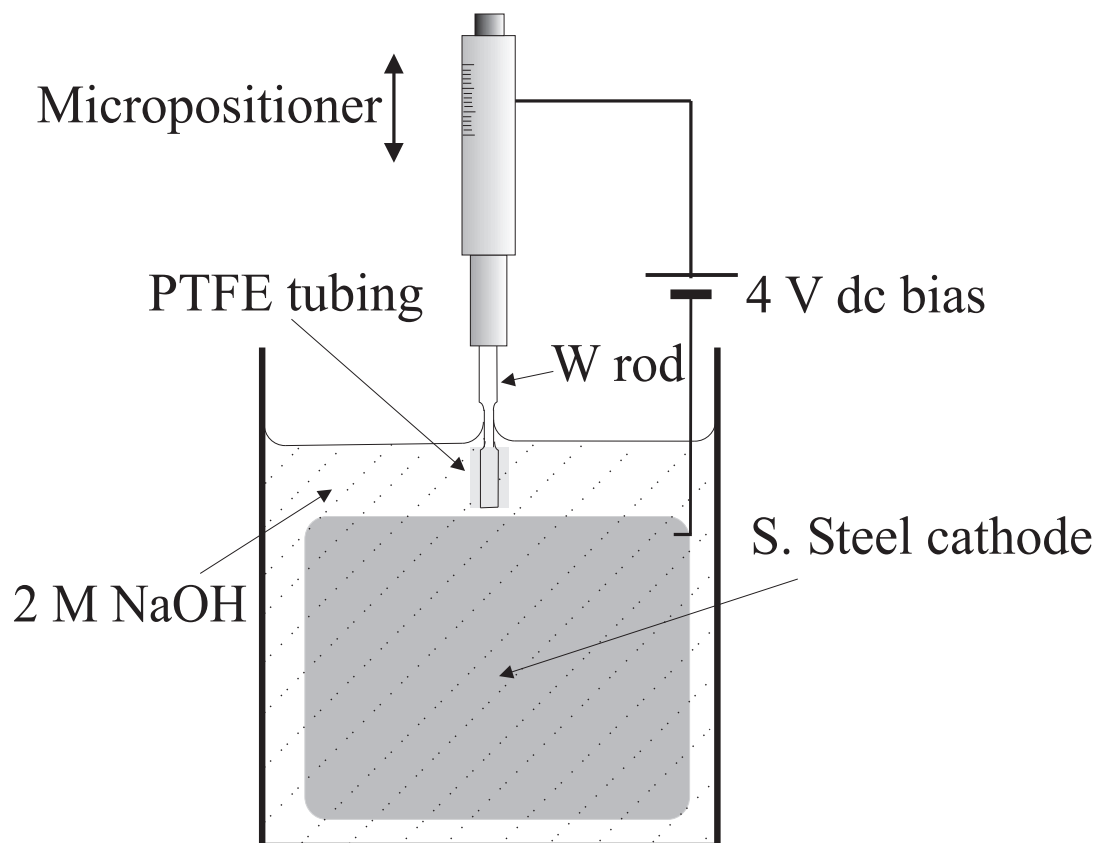


Figure 3.7. Electrochemical etching set-up used to prepare STM tips from W rods.

Chapter 4

The O/W(110) system

4.1 Sample cleaning and preparation

The sample preparation and analysis were executed in an ultra-high vacuum (UHV) multichamber system equipped with scanning tunneling spectroscopy (STM), low energy electron spectroscopy (LEED) and Auger electron spectroscopy (AES). The base pressure resided in the mid 10^{-11} Torr. The sample was prepared from a 99.995% pure tungsten crystal (Surface Preparation Laboratory, Netherlands) and was aligned to within $\pm 0.1^\circ$ of the (110) crystal plane. The surface was cleaned by repetitive cycles of annealing at $1700 \text{ K} \leq T \leq 1900 \text{ K}$ in an oxygen atmosphere of partial pressure 10^{-6} Torr for time intervals of 15 - 60 minute intervals, followed by short anneals (~ 15 sec) at 2200 K in UHV. The sample temperature was monitored using a $1\mu\text{m}$ wavelength infra-red pyrometer (Ircan, Ultimax UX-20P) with an emissivity setting of 0.23 and an estimated accuracy of $\pm 50 \text{ K}$.¹ The cleaning procedure was repeated until AES analysis indicated that contaminants (S, C and O) were eliminated and a sharp (1x1) LEED pattern was obtained. The sample was oxidized by heating to between 1000 K and 1300 K in 10^{-6} Torr for 0.5-60 min. Molecular oxygen of 4.8 N purity was introduced into the system via a precision leak valve. The STM images presented here were obtained at room temperature in constant current mode using W tips, with the sample biased with respect to the tip. Oxide overlayers were removed from the surface by a series of repeated flash-anneals to 2200 K in UHV.

¹ The estimated accuracy was due to factors such as the reflectivity of the viewport, temperature gradient across the sample and most importantly, the stray radiation from the tungsten filament of the e-beam heater.

4.2 Clean W (110)

The surface was cleaned using the method described in the previous section, namely cycles of annealing in O₂ followed by flash-anneals in UHV to temperatures in excess of 2200 K. The procedure was repeated until a clean W surface was obtained as determined by Auger and LEED analysis. A typical LEED pattern obtained from the clean surface is shown in figure 4.1 with the [001] and [1-10] directions labeled. The presence of sharp diffraction spots and low background intensity suggests that the surface is well-ordered. Many cycles of annealing were required to obtain a suitably contaminant-free surface. The chemical composition of the clean surface is shown in figure 4.2. It was evident from the Auger data that the presence of oxygen on the surface proved to be difficult to completely eliminate. However, for the purpose of oxidation studies this surface was deemed suitable as a starting point for the experiments.

Figure 4.3 shows a globally plane-fitted 500 nm x 500 nm STM image of the surface taken 90 minutes after cleaning. The surface topography is characterized by a “staircase” arrangement of terraces of average width $d = 70.5$ nm, separated by monatomic steps (see figure 4.3(a)). The average value of the step height is measured from averaging over a large number of line profiles obtained from locally-planed STM images. In this case, the measured step height is $h = 2.2 \pm 0.1$ Å, which is within 5 % of the value for the unrelaxed surface of 2.234 Å. Taking these values for the terrace width d and the step height h and applying them to the simple geometrical expression:

$$\tan \alpha = h/d$$

Yields a value for the miscut angle α of $\sim 1.4^\circ$. Using a mark on the cap of the sample holder as a reference, the direction of the step-edges in the STM images was correlated with the LEED data. It was found that the steps were aligned along the [1-10] crystallographic direction.

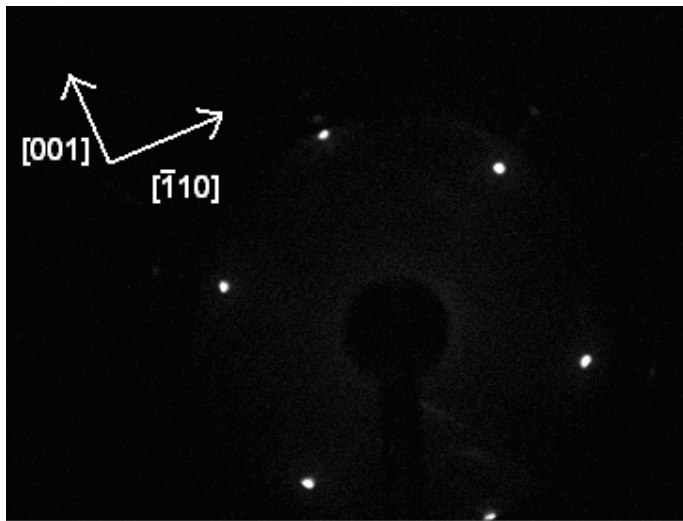


Figure 4.1. LEED pattern of the clean W(110) surface. $E_{\text{beam}} = 54 \text{ V}$.

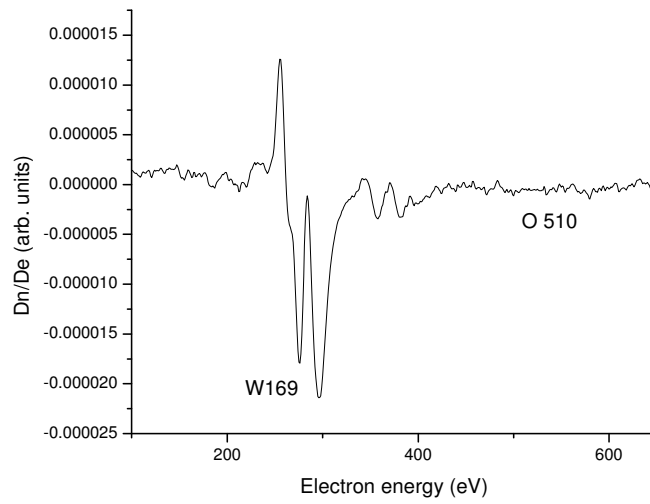


Figure 4.2. Auger spectrum of the clean W(110) surface.

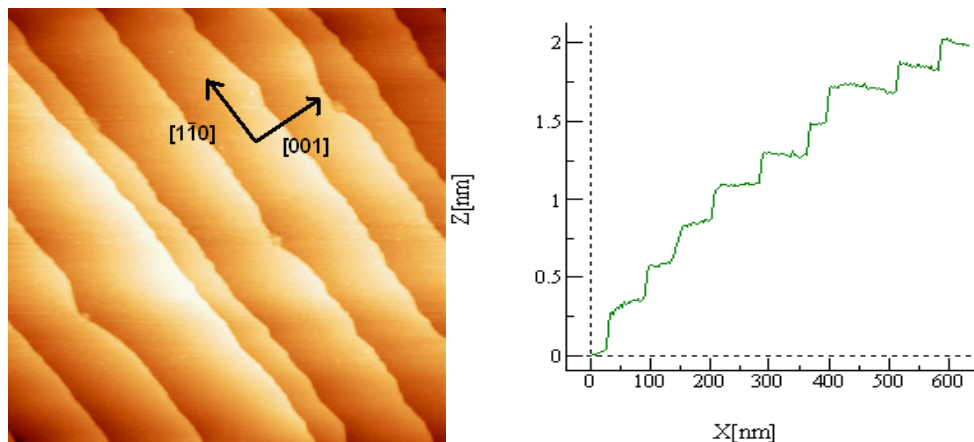


Figure 4.3. 500 nm x 500 nm STM image of the clean W(110) surface with global plane fitting. W tip. $V_{\text{bias}} = 390$ mV, $I_{\text{tunnel}} = 0.1$ nA. Right image displays a line-profile along the [001] direction indicating the “staircase” topography.

It is evident from the AES data that a certain amount of oxygen is present on the surface however, considering the nature of the experiments, oxygen is not deemed to be an obstructive impurity. Auger analysis did not indicate sulphur peaks and residual gas analysis of the UHV system, performed by previous users, attest to the absence of the element in the UHV environment. Other possible contaminants include molecular hydrogen and water, which are both prevalent in the residual gas found in stainless steel UHV systems [x, xx]. As indicated by Osing [xx], molecular hydrogen comprises the majority of the residual gas in the UHV system used during this study, with an estimated partial pressure of $P = 8 \times 10^{-11}$ mbar. This is to be expected as H_2 generally comprises the greater part of the residual gas in any stainless steel UHV system [98]. From this information it can be assumed that there is almost certainly a small amount of Hydrogen on the surface, which is undetectable by AES as a result of its weight/size. Other compounds that are likely to adsorb from the residual gas include CO and CO_2 .

4.3 W-O rows (1ML coverage @ RT) – Sample A

The exposure of W (110) to oxygen at room temperature has been widely studied [99]. Numerous coverage-dependent oxygen overlayer phases have been identified and characterized by LEED [26, 38, 39]. The three ordered phases are (2 x 1) at $\theta = 0.5$ ML, (2 x 2) at $\theta = 0.75$ ML, and (1 x 1) at $\theta = 1$ ML. The phase diagram for this adsorbate system has been carefully studied using LEED spot profile analysis [100], and is shown in figure 4.4. It

was reported that at intermediate coverages, there is the possibility of phase coexistence separated by single phase domain walls. There are a number of possible adsorption sites on W (110) as shown in figure 4.5: Top, centre, bridge and 3-fold hollow, with site occupation depending on the oxygen coverage. For a full report of ordered structures of oxygen on W (110) see Johnson et al. [40].

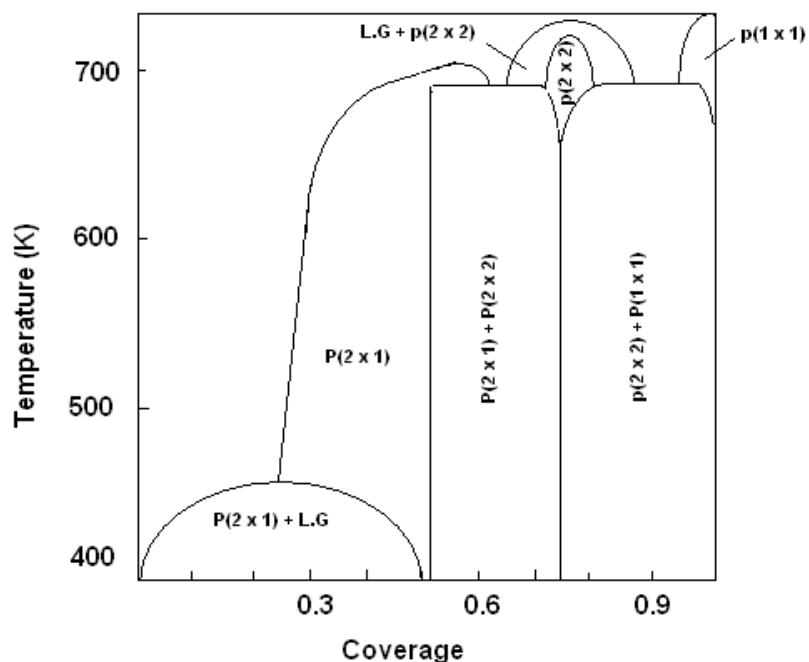


Figure 4.4. Phase diagram for O/W(110). Reproduced from [100]. L.G. stands for 2D lattice gas.

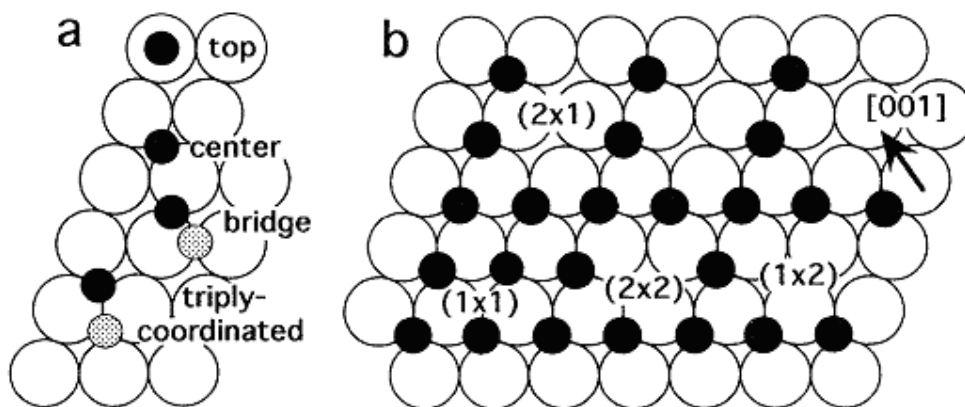


Figure 4.5. Model of oxygen adsorbed on W(110). The open circles and closed circles represent the metal and oxygen atoms respectively. (a) The adsorption sites of O on W(110).

Note the presence of the two equivalent triply coordinated sites. (b) Structure of the three ordered phases. Reproduced from [40].

Exposure of the W(110) surface to oxygen at room temperature resulted in the same sequence of LEED patterns as described by Germer and May [26]. The (1x1) oxygen overlayer structure was produced by exposing the substrate to 300 Langmuirs, 10^{-6} Torr O_2 for 5 minutes at room temperature, corresponding to a coverage of 1 ML [26]. No further adsorption occurs at room temperature [26]. The LEED pattern of the (1x1) chemisorbed oxygen structure on clean W(110) is shown in Figure 4.6. It is clear from this data that there is a (1 x 1)-O surface overlayer present. AES data confirms the increased presence of oxygen on the surface however the exact relative chemical composition cannot be accurately determined. AES analysis receives contributions from the first 10-15 atomic layers of the surface and not just the top-most layer. Considering there is only one layer of oxygen on the surface suggests that AES cannot give an accurate representation of the chemical ratios of oxygen and tungsten. It has been well documented that the W(110) surface saturates at 1 ML oxygen coverage and so it can be assumed that, under the experimental conditions used, there is only 1ML of Oxygen present. The AES data for the saturated (1 x 1) chemisorbed oxygen overlayer is shown in figure 4.7.

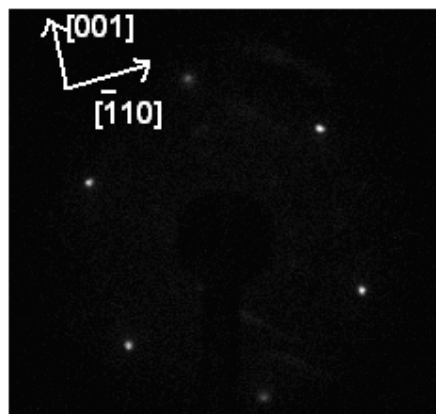


Figure 4.6. LEED image of the (1 x 1) Oxygen overlayer on W(110). Beam energy = 72 eV.

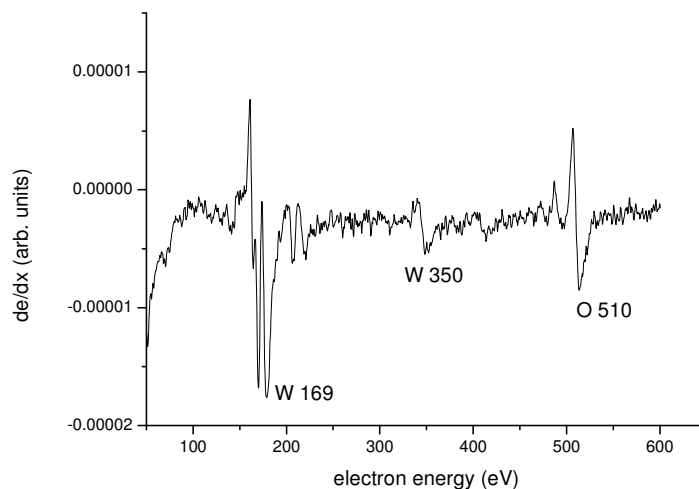


Figure 4.7. AES spectrum of the (1 x 1) oxygen overlayer structure on clean W(110). Estimated O_{510}/W_{169} ratio is 0.05.

The (1x1) structure was subsequently annealed at 1300 K in UHV for 5 minutes which resulted in a complex LEED pattern as shown in figure 4.8. The pattern shows rows of satellite spots corresponding to the two equivalent W [1 -1 3] and W [-1 1 3] directions with a periodicity of about 30 Å. This complex LEED pattern has been seen before by Bauer [39]. Figure 4.9 displays a STM image confirming the row-like structure as seen in LEED. The rows have a periodicity of 30 Å and a corrugation of < 1 Å. The average step height is 2.2 Å which shows no deviation from that of the clean W(110) surface suggesting that a 3D oxide is not formed, but rather a chemisorbed oxide layer is present. The fact that only 1ML of oxygen was absorbed onto the surface prior to annealing, suggests that the post annealed structure is not WO_2 or WO_3 as more oxygen would be required to create such products. It was discovered by Germer and May [26] that flashing W(110) in UHV to temperatures in excess of 1200 K resulted in various chemisorbed overlayer structures with increasing temperature, implying that temperatures in excess of 1200 K are required to decompose surface oxides. The anneal temperature used here is relatively low compared to the temperature required to fully remove chemisorbed oxygen (2200K) suggesting that only a small amount of oxygen is removed at this temperature.

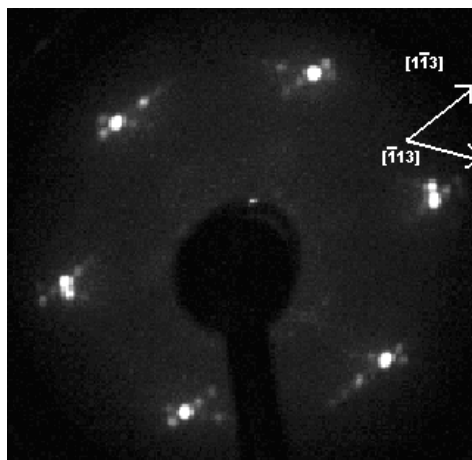


Figure 4.8. LEED image of the (1 x 1) oxygen overlayer structure on clean W(110) after annealing for 5 minutes in UHV at 1300 K

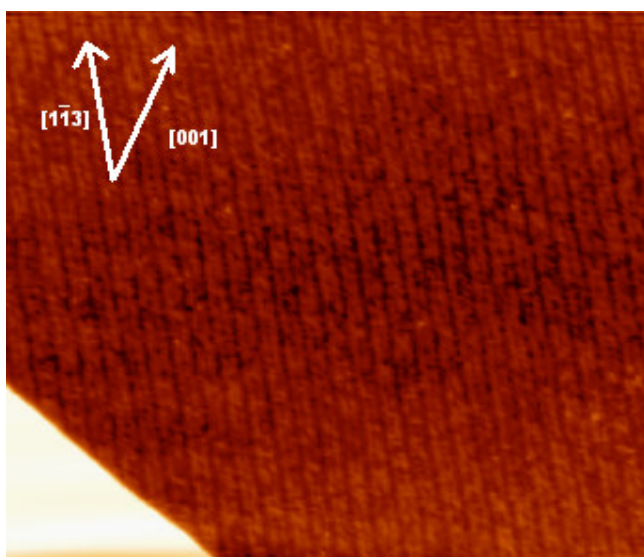


Figure 4.9. 72 nm x 61 nm STM image of the row-like structure corresponding to LEED pattern in figure 4.8. The STM image was taken with a W tip using tunnel parameters of $V_{\text{bias}} = 388$ mV, $I_{\text{tunnel}} = 0.1$ nA.

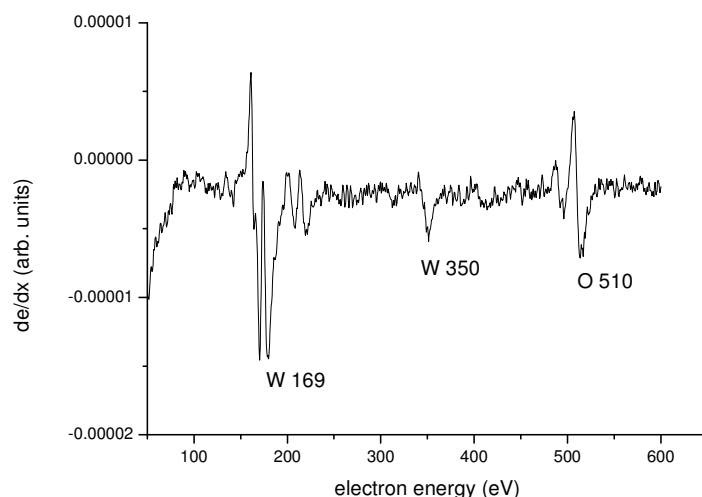


Figure 4.10. Auger spectrum of 1ML Oxygen on W(110) after 1300 k anneal in UHV. The estimated O510/W510 ratio is 0.05, which is the same as the pre-annealed W(110)-O surface.

Figure 4.10 shows the AES data obtained after the W(110) (1 x 1) – O surface was annealed to 1300 K. Quantitatively comparing this data with the Auger spectrum from the pre-anneal sample, indicates very little difference and implies that a minimal amount of oxygen has been removed from the surface during the annealing process.

A couple of models for the row structure have been formulated previously. The more recent and widely accepted model describes a structure whereby two types of (1 x 1) oxygen overlayer domains coexist on the W(110) surface. At room temperature oxygen atoms adsorb into domains of two equivalent three-fold hollow sites, separated by domain walls, that completely cover the surface. When the structure is annealed to 1300K, a small amount of oxygen desorbs preferentially at the domain walls uncovering the metal underneath, displaying the ordering of the two site-exchanged domains. The domain walls are rows of empty three-fold hollow sites spaced at regular intervals of about 33 Å and a periodicity of approximately (1 x 12) oriented along the [1-13] and [-113] directions. A schematic of the model is shown in Figure 4.11. While the STM study by Johnson et al. found the domain walls to be aligned along the W<-113> directions, Ynzunza et al. measured them to be along the W<-112> directions using photoelectron diffraction. The difference is explained by the slightly different oxygen coverages obtained in the two studies.

The LEED data indicates that the rows are in the W $[1-13]$ and $W[-113]$ directions. The orientation of the rows are obtained by measuring the angle between the rows and the $[001]$ direction.

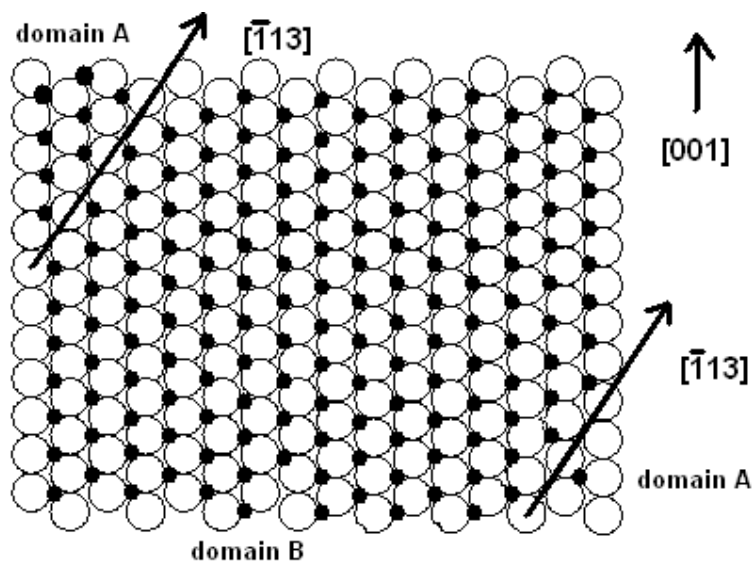


Figure 4.11. Schematic model of the (1×12) site-exchanged domain walls. Hollow circles represent metal atoms while small black balls represent adsorbed oxygen. Reproduced from [41]

Ordered phases of any adsorbate on a substrate arise as a result of the structure attempting to minimize the surface energy. The location of the adsorption site and compressive surface stress are both factors which contribute to the surface energy and thus have an effect on adsorbate ordering. In the case of O on W(110), oxygen atoms adsorb into one of two distinct triply-coordinated sites of the W(110) unit cell, giving rise to separate domains with the adsorption site exchanged. This structure entails compressive surface stress which can be somewhat relieved by annealing, giving rise to the formation of site-exchanged domain superstructures. In short, the adsorbate superstructure imaged here with STM, is simply attributed to site-exchanged domains with long range order.

Two atomically resolved images of the (1×1) oxygen overlayer structure are shown in figures 4.12 and 4.13. Both these images were obtained under similar preparation conditions with one critical difference - the annealing temperature. An effort was made to study the effect of decreasing annealing temperature on the results. The STM image in figure 4.12 was annealed at 1200 K while that in figure 4.13 was annealed at 1000 K. Note; the results presented thus far were obtained after the sample was annealed at 1300 K. It was discovered

that the width of the domain walls decreased with temperature from about three atomic spacings wide at 1200 K to one atomic spacing at 1000K. This effect was mentioned by Johnson et. al [40]. From this data it can be ascertained that at 1000 K Oxygen starts desorbing preferentially from the domain walls. A slight increase in temperature encourages further local desorption causing the domain boundaries to widen. The (1 x 1) site exchanged domain superstructure is lost with further temperature increases resulting in the well-documented ordered chemisorbed structures mentioned previously. Domains of the p(2 x 2) oxygen overlayer phase visible on the surface, which form as the sample is cooled down from 1200 K to room temperature and will be discussed in more detail in section 4.4. The edges of the (1 x 1) domains in figure 4.13. appear bright as a result of the lowered number of nearest neighbours caused by the desorption of oxygen at the domain walls.

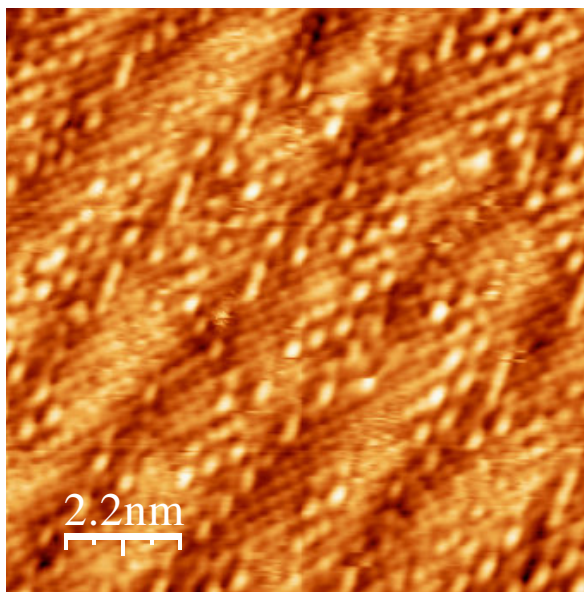


Figure 4.12. 11 nm x 11 nm STM image of the (1 x 1) site-exchanged domain annealed at 1200 K. $V_{\text{bias}} = 200\text{mV}$, $I_{\text{tunnel}} = 0.1\text{ nA}$.

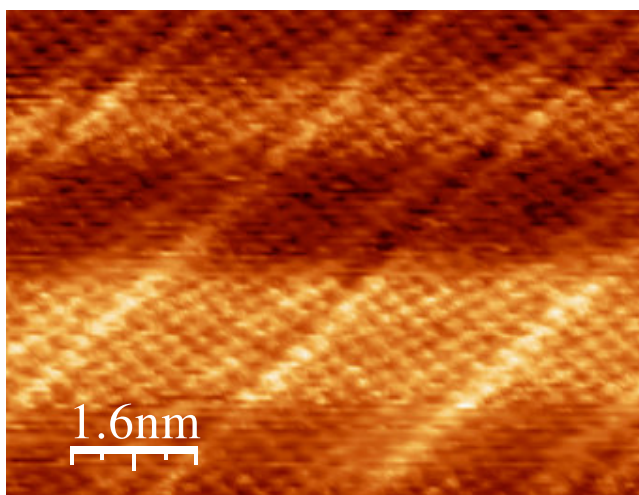


Figure 4.13. 8 nm x 6 nm STM image of the (1 x 1) site-exchanged domain annealed at 1100 K. $V_{\text{bias}} = -200\text{mV}$, $I_{\text{tunnel}} = 0.1\text{ nA}$.

4.4 The p(2 x 2) + p(1 x 1) structure

The rate at which the sample was cooled from 1300 K in UHV affected the resultant surface product. At 1300 K only oxygen is present on the surface. As the temperature was decreased from 1300 K to room temperature, STM results indicated the coexistence of the p(2 x 2) and p(1 x 1) chemisorbed oxygen phases on the surface. The phase diagram in figure 4.4 illustrates that this phase coexistence occurs when there is between ~ 0.75 ML and 1 ML of oxygen present on the surface and forms between 400 and 700 K. Temperatures in excess of 700 K produce a single phase (1 x 1) oxygen overlayer structure or a 2D lattice gas depending on coverage. When the emission current used to heat the sample was switched off instantly, effectively quenching the sample, a pure oxygen overlayer resulted with properties previously discussed, namely, the site exchanged (1 x 1) domains separated by rows of vacant three-fold hollow sites. These results have been discussed in section 4.3.

As the cooling rate was decreased², p(2 x 2) oxygen overlayer phases became apparent on the surface. Firstly, the conditions which gave rise to the (1 x 1) site-exchanged domain superstructure were repeated, see section 4.3. The emission current heating the sample was ramped down over 2 minutes in a UHV environment. STM results indicate the

² Note: The design of the e-beam heater does not permit accurate temperature control and so the actual cooling rate of the sample could not be determined. See [79] for a full analysis on the design and properties of the e-beam heater.

coexistence of $p(2 \times 2)$ -O domains and (1×1) site-exchanged domains on the $W(110)$ surface. Only very faint half-order spots were visible in the LEED pattern due to the relative scarcity of the $p(2 \times 2)$ structure with respect to the (1×1) structure. It was evident from LEED that the row structure was still present on the surface, however the separation between the rows has decreased from 30 \AA to 25 \AA .

Repeating the experiment and decreasing the cooling time to 5 minutes, i.e. ramping the emission current down over 5 minutes, resulted in further ordering of the $p(2 \times 2)$ structure. From this it can be ascertained that the longer the surface spends in the 400 to 700 K range, the range at which phase coexistence occurs, the more time the $p(2 \times 2)$ structure has to form. Figure 4.14 shows a STM image with substantial ordering and phase coexistence of the $p(1 \times 1)$ site-exchanged domain superstructure and the $p(2 \times 2)$ phase. The lattice parameters of the $p(2 \times 2)$ structure is $4.48 \text{ \AA} \times 4.48 \text{ \AA}$. LEED reveals vivid half order spots corresponding to the $p(2 \times 2)$ phase, shown in figure 4.15.

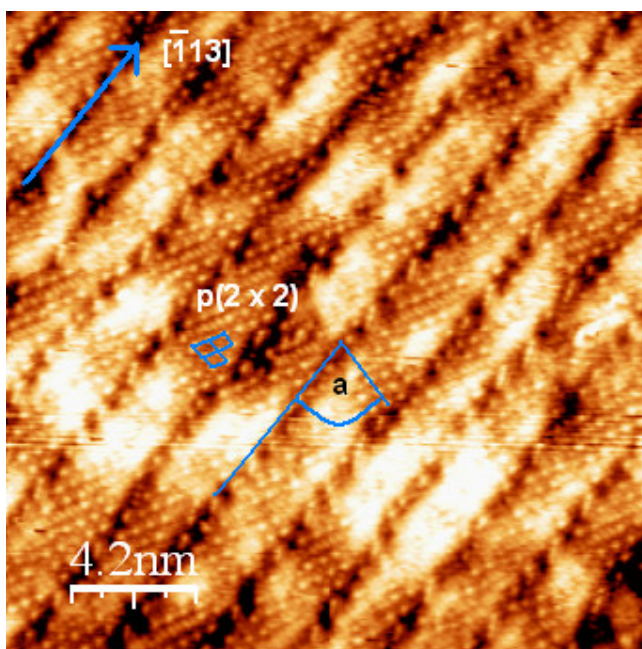


Figure 4.14. 21 nm x 21 nm STM image of the coexistent phases of $p(1 \times 1)$ site-exchanged domain superstructure and the $p(2 \times 2)$. Imaged acquired with a w tip with tunneling parameter of $I_t = 0.1 \text{ nA}$ and $V_{\text{bias}} = 0.2 \text{ V}$.

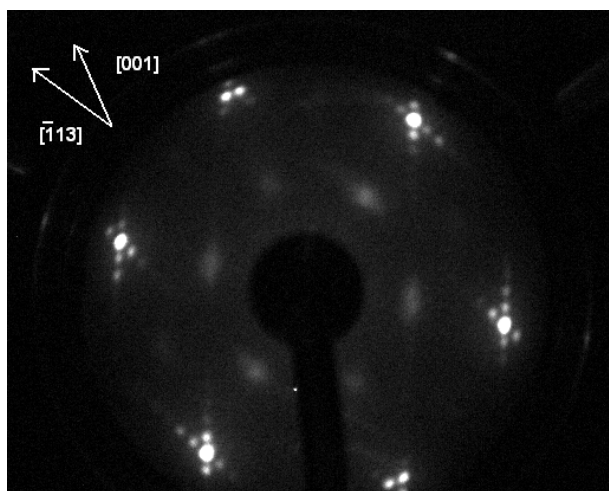


Figure 4.15. LEED image of the $p(1 \times 1)$ superstructure with half-order spots representative of the $p(2 \times 2)$ phase. Image acquired with a beam energy of

Analysis of the STM image shown in figure 4.14 reveals further downsizing of the row separation to 20 \AA . It is clear that cooling rate effects the row separation, with slower cooling rates giving rise to shorter row separation. The angle between the $[-113]$ and the close packed $[-11-1]$ direction was measured in the STM image to be 79° which is confirmed by the model displayed below in figure 4.16.

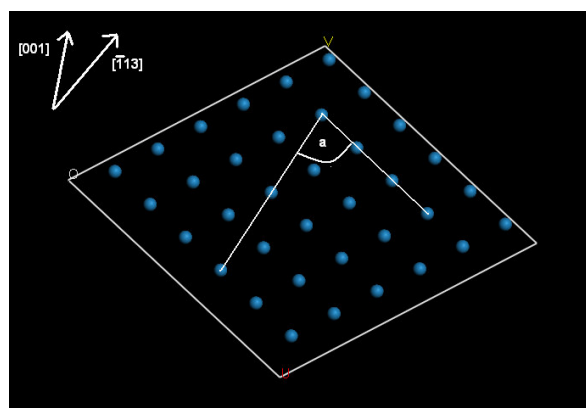


Figure 4.16. Model of the $W(110)$ surface with the angle between the $[-113]$ and the close packed directions marked.

4.5 Cooling in molecular oxygen

Adsorption of oxygen on $W(110)$ at room temperature saturates at a coverage of 1 ML. Oxygen atoms adsorb at one of two three-fold hollow sites, forming alternating (1×1) site-exchanged domains. Subsequent annealing of the oxygen saturated surface at 1300 K results

in remarkable ordering of the domains in an effort to minimize the surface energy. The cooling of this structure in UHV results in the coexistence of the p(1 x 1) site-exchanged domain superstructure and the p(2 x 2) overlayer phase with the cooling rate determining the relative abundances of each structure. In this section, the 1 ML oxygenated surface was cooled from 1300 K to room temperature in an oxygen partial pressure of 1.0×10^{-6} Torr. It will be shown that the presence of oxygen during the cooling process results in the formation of epitaxial layers of bulk oxides and that the various phases formed were dependent on the cooling rate used.

4.5.1 Metal diffusion

A fast cooling rate (30 sec.) resulted in the diffusion of metal atoms to the surface with the previously discussed rows discernable underneath. As mentioned previously, the design of the e-beam heater does not allow for accurate temperature control and so the actual cooling rate could not be determined. This is the next logical stage after the structure mentioned in section 4.4. Metal atoms rise to the surface in preparation for oxide formation. The distinguishable difference in this case is that there is now ambient oxygen present to permit oxide growth. Due to the fast cooling rate, metal atoms arriving at the surface are limited and a partially complete W-O-W trilayer is the final product. The metal atoms diffuse through the (1 x 1) site-exchanged domains as shown in figure 4.17 and considerable ordering of the metal along the direction of the rows are evident. The apparent elongation of the metal atoms could be due to a few factors: (1) There is clustering of the metal atoms in groups of two or three, (2) STM drift or (3) WO_x clusters.

A line profile of the “bright spots” shows a periodicity of 6.5 Å and a corrugation of 0.3 Å. The apparent length of the spots are ~ 3 Å.

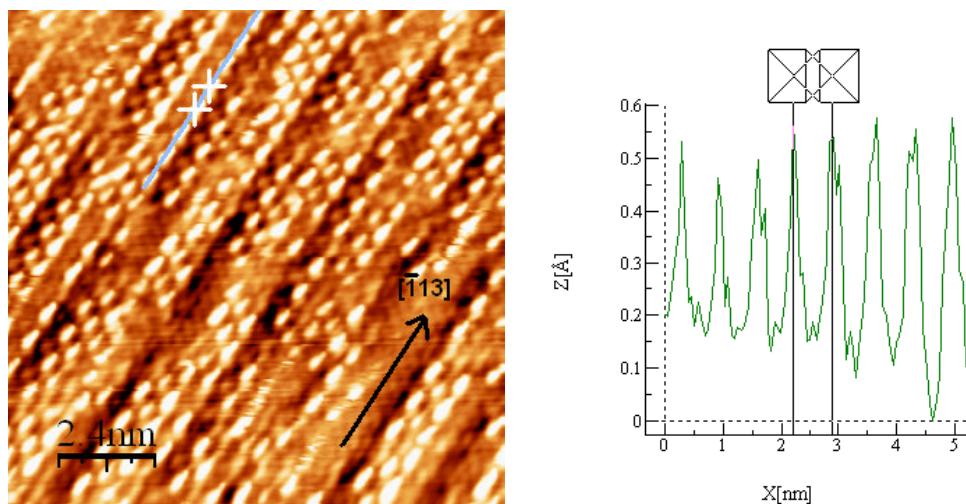


Figure 4.17. Left 12 nm x 12 nm STM image of metal atoms diffusing to the $p(1 \times 1)$ oxygen surface. Left shows a line profile with periodicity of 6.5 \AA and corrugation of 0.3 \AA . Imaged using W tip of tunneling parameters of $V_{\text{bias}} = 0.2 \text{ V}$ and $I_t = 0.1 \text{ nA}$.

An interesting discovery under the current oxidation conditions unfolded with respect to the direction of the rows, or more precisely, the orientation of the (1×1) site exchanged domains. The presence of oxygen during the cooling process resulted in faceting at the step edges as shown in figure 4.18. This is in contrast to the straight step edges apparent on clean W(110) and the those found in the system which was cooled in UHV. The step height is 2.2 \AA which shows no deviation from that of clean W(110) indicating that the structure present is not likely to be an oxide, but rather still an “incipient-oxide”, or 1 layer of oxygen sprinkled metal atoms which have diffused to the surface. The interesting discovery lies in the change in orientation of the (1×1) site exchanged domains at the newly formed peninsula-like structures extending from the steps. From this data, it appears that the direction of the steps has a direct influence on the orientation of the chemisorbed (1×1) site exchanged domains. In the center of the large terraces, the domains are found to be oriented in the familiar equivalent $[1-13]$ and $[-113]$ directions, however, at the newly formed “protrusions”, they have shifted orientation. This effect could have promising outcomes. If the orientation of the (1×1) site exchanged domains can be controlled by the direction of the steps (i.e. the cleave direction), control of the orientation of any W-O structure discovered may be obtained. It is however important to note that the shift in domain direction is only apparent at the step edges. Changing the direction of the site-exchanged domains over the entire surface would require the sample to have a large miscut angle which would give rise to a large step density. Small bright spots are apparent in the center terraces which are thought to be the nucleation W-O crystals.

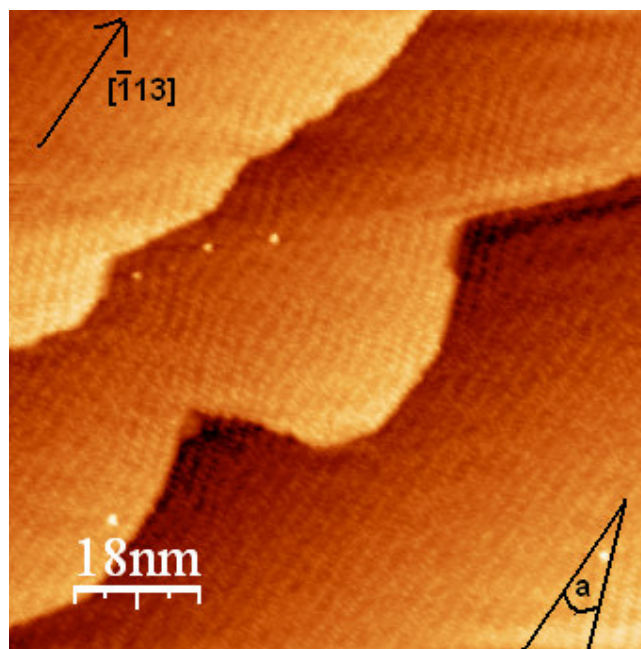


Figure 4.18. 92 nm x 92 nm STM image of step protrusions. A change in row direction is apparent at step edges and the angle, a , between the rows is 22.5° . Imaged with W tip and tunneling parameters of $V_{\text{bias}} = 0.2$ V and $I_t = 0.1$ nA.

4.5.2 W-O three dimensional Islands (Sample B)

The next two sections were studied with a different sample to that used thus far. The new sample is W(110) with a slightly different miscut angle. Specifics regarding this sample can be found in section 4.6.

Cooling the sample over 2 minutes resulted in the first signs of oxide formation in the form of three dimensional WO_x islands as shown in figure 4.19. Although no atomically resolved images were obtained, the oxide present is thought to be WO_3 with the (11-1) plane parallel to W(110) which has been reported previously by Avery [28]. The height of the islands are 3.4 \AA which is consistent with the $\text{WO}_3(11-1)$ plane separation. The islands appear to nucleate in the center of the terraces and grow in the direction of the (1 x 1) rows. The three dimensional islands are thought to be the first oxide layer due the presence of the (1 x 1) row structure (figure 4.20) and the step height being consistent with W(110). An important observation, is that the width of the (1 x 1) site-exchanged domains, are no longer regular which may reflect the disruption of the long-range interaction between the rows by the presence of the oxide epilayer. Another possible explanation for this effect may be due to a

selection of three-fold hollow vacancy sites, responsible for the row structure, becoming occupied and giving rise to the decrease in order of the (1 x 1) domains. From the line profile in figure 4.20, the island itself displays corrugation. Figure 4.21 shows a 3D image of the islands giving an indication of their height. The row structure can also be seen supporting the elongated islands. A remarkable observation is that the WO_3 crystals nucleate on the terraces and not the step edges as expected. Figure 4.19 also shows coalescence of the WO_3 islands forming large areas of the surface oxide.

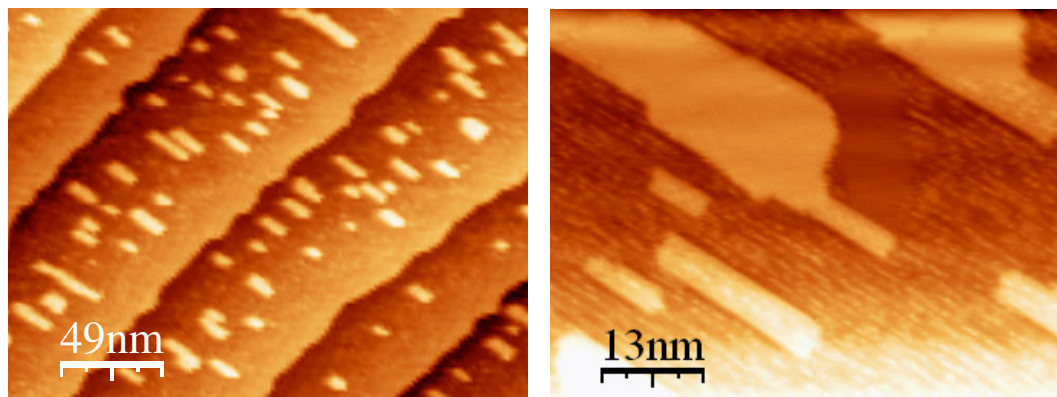


Figure 4.19. Left shows 25 nm x 19 nm STM image of the elongated WO_3 islands. Right displays the coalescence of the islands. Both images were imaged with a W tip with tunneling parameters of $V_{\text{bias}} = -0.2$ V and $I_t = 0.1$ nA.

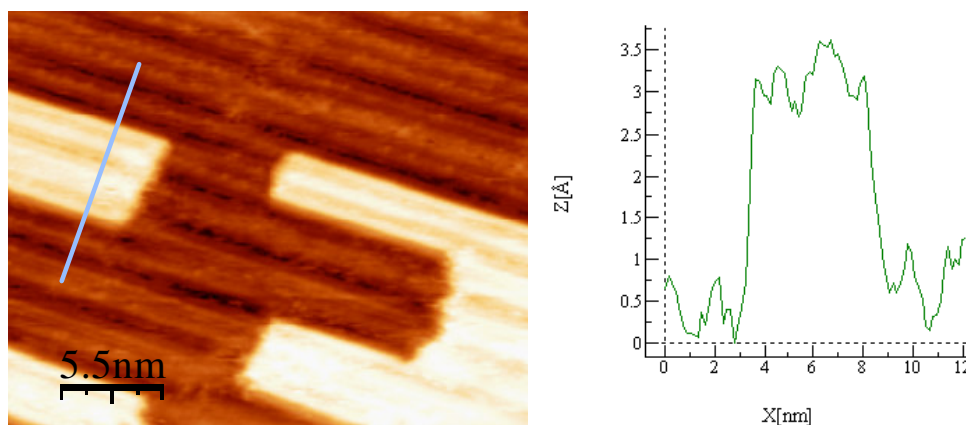


Figure 4.20. 27 nm x 220 nm STM image of WO_3 islands on the row structure. Right image displays a line profile of an island indicating the 3.4 Å corrugation associated with the (11-1)

plane separation distance of WO_3 . Imaged with W tip and parameters of $V_{\text{bias}} = -408\text{mV}$, $I_{\text{tunnel}} = 0.1\text{ nA}$

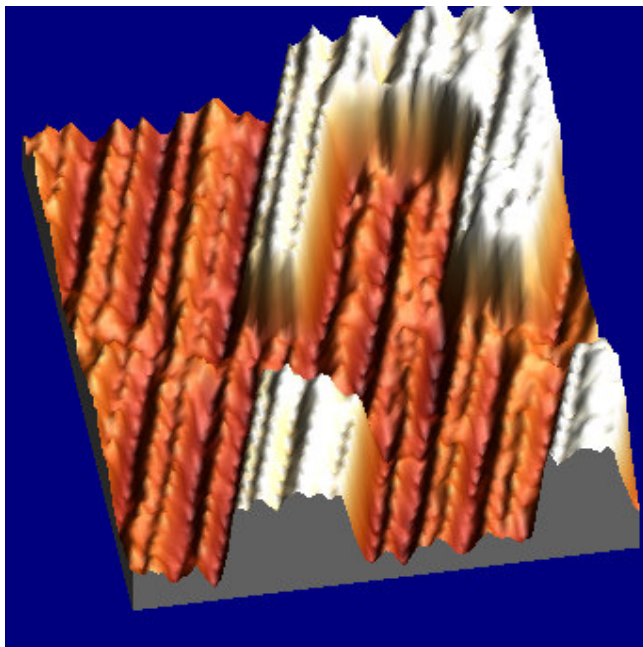


Figure 4.21. Three dimensional STM image of the WO_3 islands with the row structure visible underneath.

4.5.3 Bulk WO_3

Finally, cooling over 5 minutes in O_2 resulted in the formation of a complete WO_3 surface oxide layer shown in figure 4.22. It is clear from the STM images that WO_3 is the oxide present with (11-1) and (100) planes coexisting on the surface. Area A and B in figure 4.22 show rotated domains of the oxygen-terminated $\text{WO}_3(100)$ structure, rotated by 22.5° with respect to each other. An atomically resolved STM image of this surface is shown in figure 4.23 and the theoretical model is compared in figure 4.24. The atomic periodicity was obtained using a line profile and revealed lattice parameters of 7.6 \AA and 7.5 \AA , which satisfies the theoretical model. It was reported by Avery [28] that both these structures form at 650 K . Figure 4.25 displays the metal-terminated $\text{WO}_3(11-1)$ surface. The presence of oxygen in the temperature range $650 - 1100\text{ K}$ enables the growth of bulk oxide, with results described by Avery [28]. Various WO_3 terminations form depending on the anneal temperature however cooling the sample slowly will always produce the results shown here. The reason for this is that the sample will spend enough time at 650 K to eliminate any

structure formed at higher temperatures, and reform the structures which grow at 650 K, namely the coexistence of the $\text{WO}_3(100)$ and $\text{WO}_3(11-1)$ surfaces.

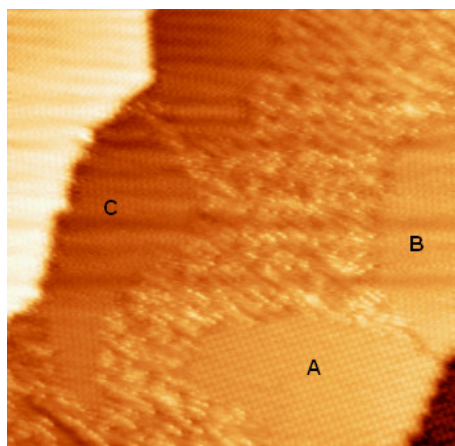


Figure 4.22. $470 \times 470 \text{ \AA}^2$ STM image of the WO_3 surface domains at the step edges. Imaged with W tip with tunneling parameters of $V_{\text{bias}} = -0.2 \text{ V}$ and $I_t = 0.1 \text{ nA}$. A, B and C represent $\text{WO}_3(100)$ domains with unfaceted $\text{WO}_3(11-1)$ in between.

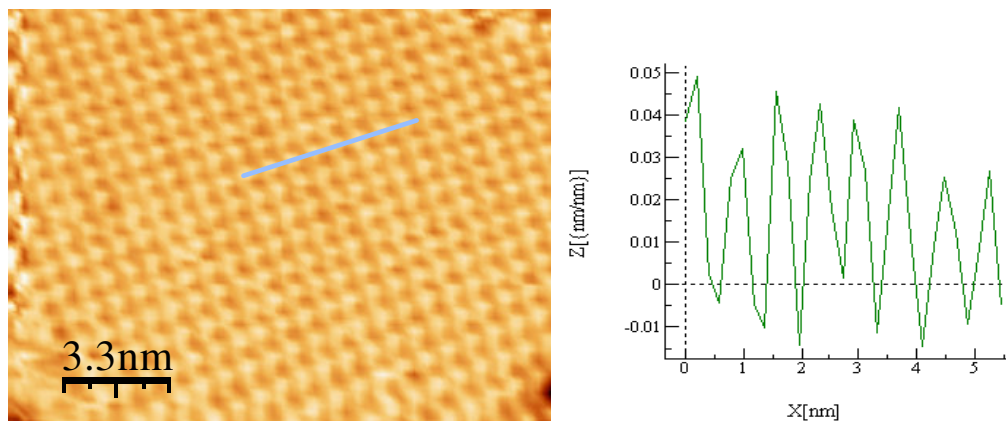


Figure 4.23. Left shows $17 \text{ nm} \times 13 \text{ nm}$ atomically resolved STM image of the (100) surface of WO_3 imaged using a W tip with tunneling parameters of $V_{\text{bias}} = -400 \text{ mV}$ and $I_{\text{tunnel}} = 0.2 \text{ nA}$. Right displays line profile of the atomic periodicity.

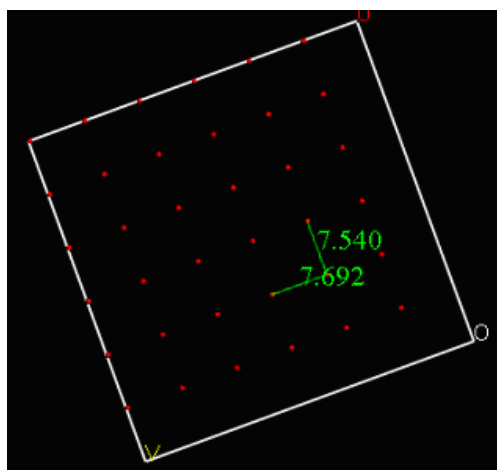


Figure 4.24. Model of the oxygen terminated (100) surface of WO_3 .

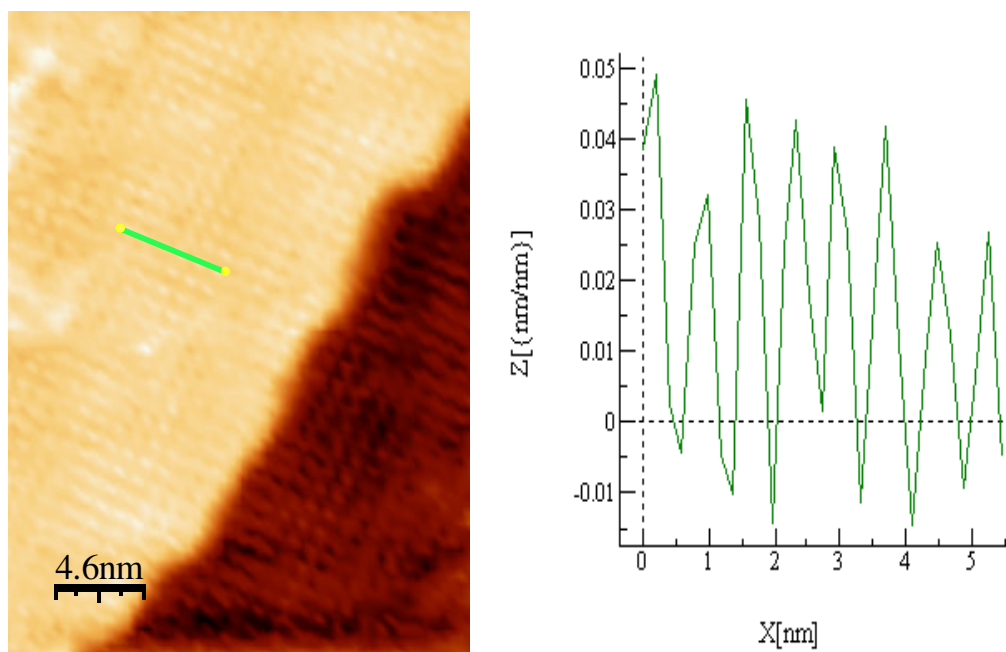


Figure 4.25. Left shows 23 nm x 32 nm STM image of the metal terminated $\text{WO}_3(11-1)$. W tip. $V_{\text{bias}} = -400$ mV , $I_{\text{tunnel}} = 0.2$ nA . Right displays line profile of the atomic periodicity.

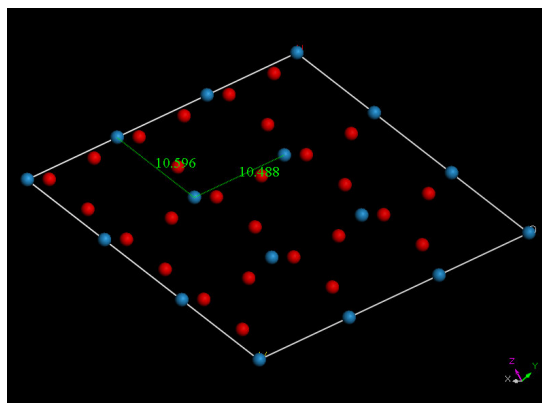


Figure 4.26. Model of the $\text{WO}_3(11-1)$ surface. Blue balls represent the metal atoms, whereas the red balls correspond to oxygen. The oxygen is the second layer.

4.6 Large miscut – Sample B

It was discovered in section 4.5.1 that the presence of molecular oxygen during the cooling process resulted in protrusion-like structures at the step edges, which in turn affected the local orientation of the (1×1) site exchanged domains. It was also postulated in this section, that if a similar sample of $\text{W}(110)$ possessing steps oriented in a different direction to those in the previous sample, the (1×1) rows would too be oriented in a different direction than the $[11-3]$ and $[-113]$ directions. Moreover, if the sample was cleaved revealing a higher density of steps, the newly oriented (1×1) rows could be present over the entire surface, due to the close proximity of the step edges.

4.6.1 Sample Preparation / Clean $\text{W}(110)$

A second sample was obtained from Surface Preparation Laboratory in the Netherlands. The cleaning and preparation conditions used were identical to those outlined in section 4.1 The clean $\text{W}(110)$ surface was obtained by cycles of annealing in O_2 and flashing to 2200 K to remove the oxide layer. This process was repeated until a minimum amount of surface impurities were detected by AES analysis as shown in figure 4.27. As before, complete removal of oxygen proved very difficult.

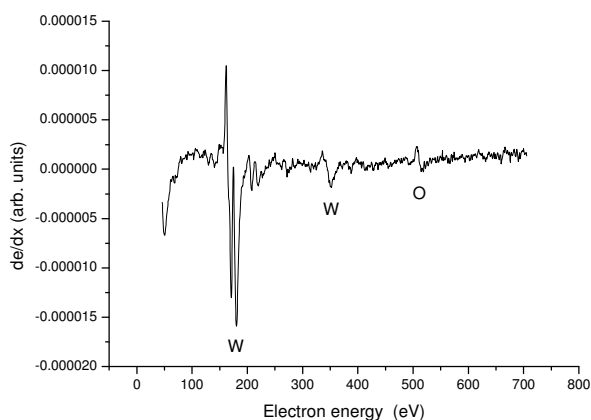


Figure 4.27. AES of clean W(110) – sample B. O510/W169 ratio is 0.02.

LEED and STM experiments of the clean surface were subsequently executed in order to discover details regarding step direction, step density and miscut angle as shown in figures 4.28 and 4.29 respectively. It was determined that the steps are oriented along the $[-110]$ direction, identical to those of sample A. A line profile study of a number of STM images on the clean surface reveals that the average step width is 24 nm. Using the knowledge that the step height of W(110) is 2.2 \AA , it can be determined trigonometrically that the miscut angle is 0.47° resulting in a much higher step density than in Sample A.

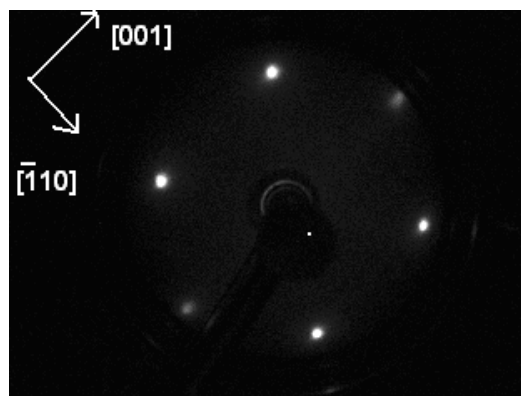


Figure 4.28. LEED image of clean W(110) surface. Beam energy = 72 eV.

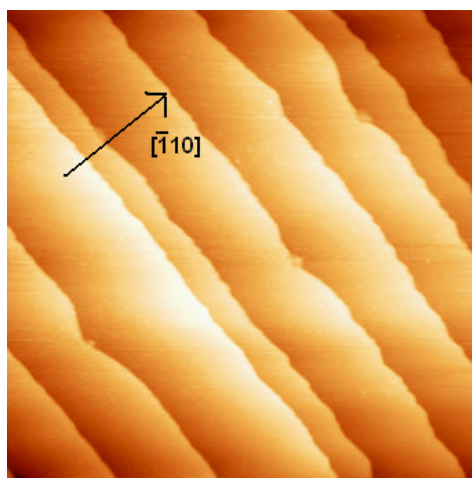


Figure 4.29. STM image of clean W(110) surface. Imaged with W tip and tunneling parameters of $I_t = 0.1 \text{ nA}$, $V_{\text{bias}} = -0.4 \text{ V}$.

Chapter 5

Summary

5.1 Conclusions

The oxidation of the (110) surface of tungsten has been studied using STM, LEED and AES. The surface was prepared by means of annealing in O₂ followed by flash annealing to temperatures in excess of 2200 K. The clean surface was subsequently exposed to O₂ partial pressure of 1x10⁻⁶ Torr for 5 minutes (300 L) at room temperature resulting in a saturated 1 ML chemisorbed oxygen overlayer. The surface reconstruction of this structure is p(1 x 1) with the oxygen atoms situated in the three-fold hollow sites of the tungsten surface. The (1 x 1) structure was then annealed at 1300 K in UHV for 5 minutes which resulted in partial desorption of oxygen and long-range ordering of site-exchanged domains. There are two domains comprising of alternating degenerate three-fold hollow site oxygen occupancy. The domain walls are rows of empty three-fold hollow sites spaced at regular intervals of 33 Å and a periodicity of approximately (1 x 12) oriented along the [1-13] and [-113] directions. The width and spacing of the rows varied according to the anneal temperature, which is also thought to be the reason behind the discrepancy between some documented results indicating a slight variation in row direction to [1-12] and [-112]. Cooling conditions from 1300 K depicted the final surface product. Cooling in UHV resulted in the structure previously mentioned, however more oxygen desorbed at slower cooling rates and the (2 x 2) oxygen reconstruction was consequently apparent. Cooling in an O₂ environment inhibited oxide growth, with anneal temperature and cooling rates again being the control factors at constant partial pressure. W-O nanoparticles, WO₃ three-dimensional islands and full development of WO₃ (100) and WO₃ (11-1) surfaces formed with decreasing cooling rates respectively. The purpose of this study was to examine the W (110)-O system as a possible template for the self-assembly of nanostructures. The rows formed at the domain walls of the site-exchanged

domain structure may give rise to preferential adsorption of adsorbates and shows high potential for self-assembly.

5.2 Further work

One of the main issues with growing nanowires on the template discussed is that the substrate is conducting rendering a structure situated on the surface useless. Tungsten trioxide is semiconducting however the site-exchanged domain structure is not a fully formed oxide but rather an incipient to oxide formation. It is clear from STM data that the surface is conducting. In order to make use of self-assembled metallic nanostructures, an insulating or semiconducting substrate will be required. It is for this reason that it will be important to grow the tungsten (110) surface on an insulating substrate. A strong candidate for such a substrate is that of Al_2O_3 (11-20). It has been shown that epitaxial growth of W(110) occurs on this surface, however obtaining a sufficiently thin metal layer to retain its insulating properties may be an issue. A second major area of future study involves the deposition of various metallic and semiconducting films on the site-exchanged domain super structure. If materials such as gold, iron, germanium etc.. grew preferentially at the domain walls, self-assembled nanowires could emerge.